Journal of Geophysical Research: Atmospheres

Key Points:
- Aerosol layers observed in the free troposphere are likely due to mean vertical motions associated with synoptic-scale convergence.
- Spatial grid spacing in global climate model too coarse to adequately resolve mean vertical motions associated with aerosol layers.
- Many characteristics of the observed aerosol layers can be reproduced by models given sufficient spatial resolution.

Model representations of aerosol layers transported from North America over the Atlantic Ocean during the Two-Column Aerosol Project

Jerome D. Fast[1], Larry K. Berg[1], Kai Zhang[1], Richard C. Easter[1], Richard A. Ferrare[2], Johnathan W. Hair[2], Chris A. Hostetler[2], Ying Liu[1], Ivan Ortega[3], Arthur Sedlacek III[4], John E. Shilling[1], Manish Shrivastava[1], Stephen R. Springston[4], Jason M. Tomlinson[1], Rainer Volkamer[3], Jacqueline Wilson[1], Rahul A. Zaveri[1], and Alla Zelenyuk[1]

[1]Pacific Northwest National Laboratory, Richland, Washington, USA, [2]NASA Langley Research Center, Hampton, Virginia, USA, [3]Department of Chemistry, Colorado University, Boulder, Colorado, USA, [4]Brookhaven National Laboratory, Upton, New York, USA

Abstract The ability of the Weather Research and Forecasting model with chemistry (WRF-Chem) version 3.7 and the Community Atmosphere Model version 5.3 (CAM5) in simulating profiles of aerosol properties is quantified using extensive in situ and remote sensing measurements from the Two-Column Aerosol Project (TCAP) conducted during July of 2012. TCAP was supported by the U.S. Department of Energy's Atmospheric Radiation Measurement program and was designed to obtain observations within two atmospheric columns; one fixed over Cape Cod, Massachusetts, and the other several hundred kilometers over the ocean. The performance is quantified using most of the available aircraft and surface measurements during July, and 2 days are examined in more detail to identify the processes responsible for the observed aerosol layers. The higher-resolution WRF-Chem model produced more aerosol mass in the free troposphere than the coarser-resolution CAM5 model so that the fraction of aerosol optical thickness above the residual layer from WRF-Chem was more consistent with lidar measurements. We found that the free troposphere layers are likely due to mean vertical motions associated with synoptic-scale convergence that lifts aerosols from the boundary layer. The vertical displacement and the time period associated with upward transport in the troposphere depend on the strength of the synoptic system and whether relatively high boundary layer aerosol concentrations are present where convergence occurs. While a parameterization of subgrid scale convective clouds applied in WRF-Chem modulated the concentrations of aerosols aloft, it did not significantly change the overall altitude and depth of the layers.

1. Introduction

While the performance of aerosol predictions has improved over the past few decades, many uncertainties, associated with processes that are not fully understood and the representation of processes that affect the aerosol life cycle in models, remain. These uncertainties are manifested as large variations in global climate model predictions of aerosol mass and consequently aerosol radiative forcing as indicated by recent Aerosol Comparison between Observations and Models (AeroCom) activities [e.g., *Myhre et al.*, 2013; *Schulz et al.*, 2006; *Textor et al.*, 2006]. In addition, these models do a poor job in representing the vertical distribution of aerosols that have been shown to be an issue in radiative forcing calculations. For example, *Schwarz et al.* [2013] used the High-performance Instrumented Airborne Platform for Environmental Research (HIAPER) Pole-to-Pole Observations (HIPPO) research aircraft data [*Wofsy et al.*, 2011] to quantify the ensemble mean black carbon among the AeroCom global models and found that the models are about a factor of 3, 7, and 15 higher than observed below 500 hPa, between 500 and 250 hPa, and between 250 and 150 hPa, respectively. *Zarzycki and Bond* [2010] showed that black carbon contributes to 50% of the forcing above low clouds, where higher uncertainties in global model predictions of black carbon likely affect estimates of aerosol radiative forcing. *Samset et al.* [2013] found that variations in radiative forcing among the AeroCom models are likely due to differences in the predicted vertical profiles of black carbon. Simulating the aerosol life cycle is challenging not only for climate models but also for regional-scale air quality models that typically use more complex treatments of aerosol chemistry and higher spatial resolution [e.g., *Feng et al.*, 2016; *Im et al.*, 2015].

There are diverse reasons for the errors in the predicted vertical distribution of aerosols, such as uncertainties in anthropogenic and biogenic emissions [e.g., *Smith et al.*, 2011; *Bond et al.*, 2013], a lack of key knowledge

needed to constrain aerosol formation processes such as those associated with secondary organic aerosols [e.g., *Tsigaridis et al.*, 2014; *Hodzic et al.*, 2015; *Shrivastava et al.*, 2015], and inadequate horizontal and/or vertical resolution [e.g., *Stroud et al.*, 2011; *Wainwright et al.*, 2012]. Errors in aerosol predictions are also often the result of error propagation of meteorological and trace gas quantities. For example, uncertainties in cloud predictions affect vertical transport of aerosols and trace gases within clouds [e.g., *Barth et al.*, 2007], wet removal [e.g., *Croft et al.*, 2012; *Wang et al.*, 2013], and photochemical processes below and above clouds [e.g., *Liu et al.*, 2006]. In the cloud-free environment, uncertainties in simulated boundary layer depth and turbulent mixing affect aerosol and precursor concentrations as well as chemical production rates and uncertainties in simulated temperature profiles that affect the buoyancy and injection height of biomass burning plumes [e.g., *Walter et al.*, 2016]. There are also limited comprehensive sets of in situ measurements of aerosol microphysical and optical properties aloft needed to evaluate models, compared to the amount of data collected at the surface. In situ measurements of aerosol properties aloft are primarily available from research aircraft deployed during short-term field campaigns [e.g., *Schwarz et al.*, 2010a; *Heald et al.*, 2011]. Satellites do provide larger spatial coverage of aerosol distributions; however, information on their vertical variations is limited to extinction and backscatter [e.g., *Koffi et al.*, 2012] that are not directly comparable to mass, size, and composition predicted by aerosol models.

There are several processes that transport aerosols from the surface into the free troposphere. During the day, aerosols that are emitted into or formed within the boundary layer are largely contained within that layer. After sunset, the convective boundary collapses and a residual layer forms that is decoupled from the near-surface, shallow stable nocturnal layer [*Stull*, 1988]. If the convective boundary layer the following day is shallower than that in the previous day, part of the aerosols in the residual layer essentially becomes part of the lower free troposphere. Sea breeze [*Verma et al.*, 2006; *Angevine et al.*, 2006; *Dacre et al.*, 2007] and terrain-induced circulations [e.g., *Lu and Turco*, 1994; *Fast et al.*, 2014; *De Wekker and Kossmann*, 2015] are local and mesoscale processes that can quickly transport near-surface aerosols into the free troposphere; however, global models with their coarse spatial resolution do not adequately resolve these circulations. Mean rising and sinking motions resulting from synoptic-scale convergence and divergence also vertically transport aerosols, but at a relatively slow rate. Cloud-scale vertical motions also vertically transport aerosols in the atmosphere. Shallow clouds entrain boundary layer aerosols at cloud base that are then transported upward by thermals [e.g., *Berg et al.*, 2009]. As these clouds evaporate, interstitial aerosols and aerosols formally in cloud droplets remain in the lower troposphere. For deep convection, strong vertical motions can transport aerosols from the boundary layer into the upper troposphere and lower stratosphere [e.g., *Barth et al.*, 2015]. Strong downdrafts in these cells can also transport air with lower aerosol concentrations and higher ozone concentrations [e.g., *Gerken et al.*, 2016] from the upper troposphere toward the surface.

Once in the free troposphere, aerosols are decoupled from the boundary layer and no longer subject to dry deposition and near-surface emissions. Instead, they become subject to long-range transport by the higher wind speeds in the free troposphere and are removed from the atmosphere only by wet scavenging and evaporation into the gas phase. Outside of clouds, convergence and divergence associated with synoptic circulations that control rising and sinking motions become relatively more important than in the boundary layer. While mean vertical velocities are small compared to the horizontal winds, they can still vertically transport aerosols several kilometers over periods of hours to days. Most notable are the "conveyor belts" that are areas of rising motions ahead of cold fronts that transport trace gases and aerosol upward [e.g., *Parrish et al.*, 2000; *Esler et al.*, 2003; *Cooper et al.*, 2004]. Stratiform and convective clouds often form in these areas of rising motions. If those clouds are precipitating, wet scavenging will remove a portion of the aerosols. Conversely, large-scale sinking motions (subsidence) associated with high-pressure systems can slowly transport aerosol from the free troposphere down toward the boundary layer [e.g., *Lugauer et al.*, 1998; *McKendry et al.*, 2001; *Reidmiller et al.*, 2009]. In addition to mean vertical motions, turbulence can act to disperse aerosol plumes [e.g., *Dacre et al.*, 2015], but turbulent mixing in the free troposphere is usually much weaker than the boundary layer and is often sporadic.

While the processes affecting the vertical distribution of aerosols in the atmosphere are fairly well known, the reasons for the poor performance in simulating them by models have received relatively little attention [e.g., *Kipling et al.*, 2016]. To address this issue, we perform simulations with a regional scale and a global model to simulate the vertical distribution of aerosol properties observed during the recent Two-Column Aerosol Project (TCAP) field campaign conducted in the vicinity of Cape Cod, Massachusetts. As described by *Berg*

et al. [2016], two research aircraft were deployed during July 2012, and measurements obtained by the aircraft revealed the presence of multiple aerosol layers. Layers in the free troposphere were found to contribute up to 60% of the total aerosol optical thickness (AOT) within the atmospheric column. There was also spatial and day-to-day variability in the aerosol chemical composition and optical properties associated with the layer. We use measurements collected by the research aircraft to assess the model performance in simulating vertical profiles of aerosol mass, composition, size, and optical properties. The measurements and the simulation results are analyzed to identify likely causes for errors in the simulated aerosol layers. The regional and global models are also compared to illustrate how resolution affects the prediction of the vertical distribution of aerosols. The measurements and models are also used to show that the layers observed during TCAP are primarily the result of mean vertical motions associated with synoptic systems, although vertical transport, aqueous chemistry, and wet removal in convective clouds modulate the concentrations of aerosols in those layers.

Section 2 describes the TCAP measurements and the configuration of the Weather Research and Forecasting model with chemistry (WRF-Chem) and Community Atmosphere Model version 5.3 (CAM5) models used in this study. Our objective is not to determine which model performed better but to illustrate the types of uncertainties in aerosol predictions associated with different spatial resolutions and complexity of the microphysical treatment of aerosols. In section 3.1, we first present the overall differences in the simulated vertical distribution of aerosols in relation to the measurements during July 2012. We show that the higher resolution WRF-Chem simulation produces more aerosol layers in the free troposphere than CAM5 and thus the fraction of AOT in the free troposphere is closer to the observed lidar measurements. This is followed by more detailed analyses of two cases in sections 3.2–3.53.2 to 3.5: one aircraft flight period with large (17 July) and one with small (22 July) aerosol concentrations aloft. For each case, we present an evaluation of the simulated aerosol concentration, composition, and size (sections 3.2 and 3.4) as well as an analysis of the processes contributing to aerosol layers in the free troposphere (sections 3.3 and 3.5). Both models are able to produce some of the vertical structure associated with observed aerosol layering and we demonstrate that the free troposphere aerosol layers are due primarily to the larger synoptic-scale mean vertical motions in the higher-resolution simulation that transports boundary layer aerosols several kilometers upward. An assessment of how a new convective parameterization influences the simulated vertical distribution of aerosols is also presented in section 3.6 and we find that this mechanism impacts aerosol concentrations but not the altitude and depth of aerosol layers. Section 4 discusses the likely sources of model errors contributing to the vertical distribution of aerosols and our primary findings are summarized in section 5.

2. Approach

2.1. TCAP Measurements

The TCAP field campaign was conducted from July 2012 through June 2013 and includes two aircraft Intensive Observation Periods (IOPs), one during July of 2012 and another one during February 2013. The goal of the aircraft IOPs was to sample aerosol microphysical properties in two columns; one fixed column near the Cape Cod National Seashore's Highlands Center on the eastern shore of Cape Cod, Massachusetts and another movable column several hundred kilometers over the Atlantic Ocean. Details of the TCAP campaign objectives, instrumentation, and measurement strategy are described by *Berg et al.* [2016]; therefore, we describe only the information relevant to the current modeling study.

To obtain vertical profiles of aerosol properties, the U.S. Department of Energy's (DOE) Atmospheric Radiation Measurement (ARM) Aerial Facility (AAF) Gulfstream-1 (G-1) [*Schmid et al.*, 2014] and the National Aeronautics and Space Administration (NASA) Langley King Air were deployed during July 2012 (phase one—the focus of this study) while only the G-1 was deployed during February 2013 (phase 2). In situ meteorological, trace gas, and aerosol property measurements were collected by numerous instruments on the G-1. The aerosol instruments within the G-1 cabin included a Droplet Measurement Technology (DMT) Single Particle Soot Photometer (SP2) [*Moteki and Kondo*, 2007; *Schwarz et al.*, 2006], an Aerodyne High-Resolution Time-of-Flight Aerosol Mass Spectrometer (HR-ToF-AMS, i.e., AMS) [*DeCarlo et al.*, 2006; *Jayne et al.*, 2000], and a single-particle mass spectrometer (miniSPLAT) [*Zelenyuk et al.*, 2015]. TCAP was the first deployment of miniSPLAT, which is miniaturized, thus more suitable for aircraft operations version of the SPLAT II instrument [*Zelenyuk et al.*, 2009] that obtains mass spectra and size of hundreds of thousands of individual particles.

Externally pylon-mounted aerosol instruments included a DMT Ultra-High Sensitivity Aerosol Spectrometer Airborne (UHSAS-A, size range 0.06–1 µm), Passive Cavity Aerosol Spectrometer Probe (PCASP, size range 0.13–3 µm), and the Cloud Aerosol Spectrometer (CAS, size range 0.6 to >10 µm) contained within the Cloud, Aerosol, Precipitation Spectrometer (CAPS) probe. The anti-ice inlet heaters were enabled on all flights for the PCASP and UHSAS, and therefore, the measured aerosol size distributions are considered dry. The CAS measurements were at ambient relative humidity (RH). The size distributions from these three external probes are merged and smoothed to generate a continuous aerosol size distribution from 0.06 µm to greater than 10 µm [*Kassianov et al.*, 2015].

The King Air deployed the second-generation High Spectral Resolution Lidar (HSRL-2), that is an advanced version of the airborne HSRL-1 instrument [*Hair et al.*, 2008; *Müller et al.*, 2014]. TCAP was the first deployment of the HSRL-2 instrument that obtained vertical profiles of backscatter, extinction, and depolarization at three wavelengths (355, 532, and 1065 nm) from near the surface up to 7.5 to 8.5 km. Aircraft operations were conducted between 09 and 15 local solar time on 10 generally cloud-free days: 9, 13–15, 17, 18, 21–23, and 25 July.

In addition to the aircraft measurements, TCAP included a yearlong deployment of the ARM Mobile Facility (AMF) [*Mather and Voyles*, 2013] at the Highlands Center that provided observations of the seasonal variations in aerosols [*Titos et al.*, 2014] and clouds over northern Cape Cod. The AMF includes over 46 instruments or instrument systems. While some of the measurements began on 3 July, most of the instrumentation became operational by 9 July, the first day of aircraft sampling. In this study we utilize measurements of black carbon from an SP2, aerosol composition from an Aerosol Chemical Mass Spectrometer (ACSM) [*Ng et al.*, 2011] and trace gas measurements of O_3 (Thermo Fisher Model 49i Ozone Analyzer), NO, and NO_2 (modified Thermo Scientific Model 42i TLE), CO (Los Gatos ICOS Analyzer), and SO_2 (Thermo Fisher Model 43i-TLE SO2 Analyzer). A Light Emitting Diode-Cavity Enhanced-Differential Optical Absorption Spectroscopy (LED-CE-DOAS) instrument [*Thalman et al.*, 2015; *Thalman and Volkamer*, 2010] was also deployed to measure glyoxal and NO_2. Radiation measurements were also made, including those from a Multifilter Rotating Shadowband Radiometer (MFRSR) instrument that were used to obtain aerosol optical depth (AOD) at multiple wavelengths during periods of few clouds [*Kassianov et al.*, 2013]. The multiday variations in these quantities are used to put the aircraft measurements into a broader context.

The flight patterns during the first phase of TCAP are shown in Figure 1. For each flight, the King Air repeated a simple back-and-forth pattern at ~9 km mean sea level (msl) over the G-1. All of the flights were anchored at one end to the AMF site. Here we define the "Cape Cod Column" to be the aircraft measurements within ~80 km of the AMF site. The second "Maritime Column" located a couple of hundred kilometers east of Cape Cod was selected based on wind direction and expected transport of aerosols from land. On some days, the aircraft sampled gradients in aerosol properties along the direction of transport, while on other days the aircraft sampled gradients in aerosol properties across the ambient wind direction. The columns of measured meteorological, trace gas, and aerosol properties were obtained by the G-1 flying at several constant altitudes, from a hundred meters above the ocean surface up to ~4 km msl. The exact altitudes varied for each flight and were selected in real time using guidance from the King Air operators using measurements from the HSRL-2. When layers of aerosols were detected by the HSRL-2, the King Air flight crew guided the G-1 aircraft to the altitudes of those layers.

As described in *Berg et al.* [2016], the measurement strategy was successful in that the G-1 was able to sample aerosol layers in the free troposphere above the residual layer transported over the ocean. Without the HSRL-2 as guidance, it would have been more difficult to find and sample those aerosol layers.

2.2. WRF-Chem Description

To better understand the formation mechanisms associated with the aerosol layers, version 3.7 of the WRF-Chem community model [*Grell et al.*, 2005; *Fast et al.*, 2006] is used to simulate the evolution of aerosols over North America and their transport over the TCAP sampling domain. Table S1 in the supporting information lists the specific physical parameterizations used in this study that are also available to the public in version 3.8 of the model. Gas-phase chemistry and aerosol chemistry, thermodynamics, and kinetic gas particle partitioning for inorganic species are simulated using the SAPRC-99 photochemical mechanism [*Carter*, 2000a, 2000b] coupled with the Model for Simulating Aerosol Interactions and Chemistry (MOSAIC) module
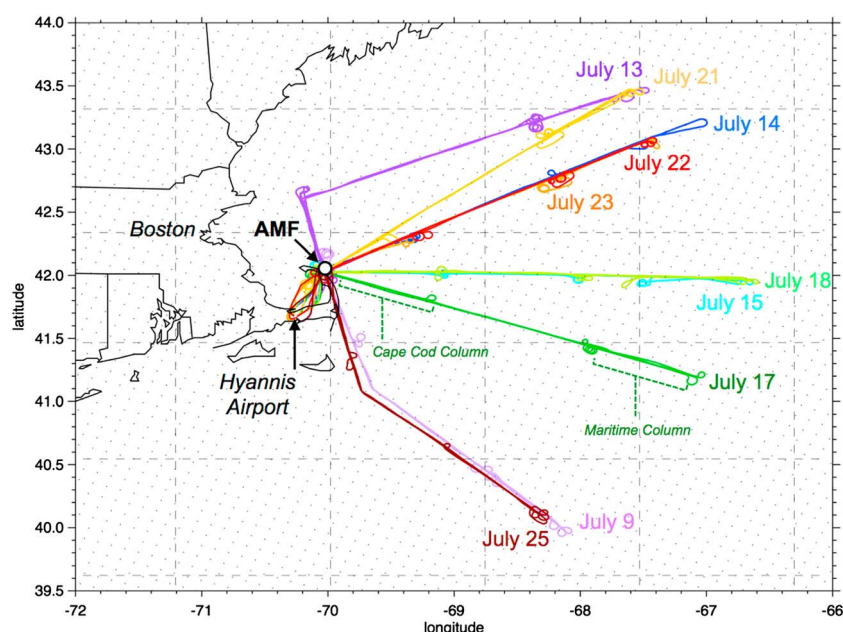
Figure 1. Flights paths of the G-1 and King Air aircraft during the TCAP campaign along with the AMF surface measurement site on Cape Cod, Massachusetts. The dashed lines denote the grid cell boundaries used by the CAM5 model and the dots denote the corners of the grid cells used by the WRF-Chem models.

[*Zaveri et al.*, 2008]. MOSAIC uses eight size bins to represent the aerosol size distribution between 39 nm and 10 µm dry diameter; both interstitial and cloud-borne aerosols are treated. A simplified two-product volatility basis set (VBS) parameterization [*Shrivastava et al.*, 2011] is used to simulate equilibrium secondary organic aerosol (SOA) formed by the oxidation of semivolatility and intermediate-volatility (S/IVOC) precursors emitted from anthropogenic and biomass burning sources with updates on the yields of SOA from biogenic sources reacting with O_3, and OH and NO_3 radicals, as described by *Shrivastava et al.* [2013]. The SOA predicted by the simplified two-product VBS was aligned to a complex multigenerational nine-species VBS approach by reducing the reaction rate of S/IVOC precursors with OH radicals to compensate for the large decrease in volatility of organic vapors, as described by *Shrivastava et al.* [2011].

WRF-Chem includes interactions between aerosols, radiation, and clouds that account for the direct, semidirect, and indirect effects [*Gustafson et al.*, 2007; *Chapman et al.*, 2009], but they are not included in this study. Resolved clouds, however, do affect aerosols through aqueous-phase chemistry in hydrometeors and wet removal. Resuspension of aerosols from evaporating rain is not considered. We use a new parameterization of subgrid scale clouds, called KF-CuP [*Berg et al.*, 2015], which includes the treatment of vertical transport of trace gases and aerosols, aqueous chemistry, wet removal, and aerosol effects on cloud drop number. This new treatment modifies the Kain-Fritsch [*Kain and Fritsch*, 1990; *Kain*, 2004] ad hoc trigger function with one linked to boundary layer turbulence using the cumulus potential (CuP) scheme [*Berg and Stull*, 2005; *Berg et al.*, 2013]. Treating the aerosol effects in parameterized, subgrid scale clouds is important when the grid spacing is relatively large (greater than a few kilometers) and does not explicitly resolve shallow or deep convection. Many models include treatments for vertical transport of trace gases and aerosols in parameterized clouds, but few models account for the other types of cloud-aerosol interactions.

The model domain encompasses much of North America as shown in Figure 2a using a horizontal grid spacing of 36 km. A nested domain that uses a grid spacing of 12 km is used over the northeastern U.S. and southeastern Canada. A stretched vertical coordinate that uses 73 grid levels extends up to ~14 km above ground level (agl), with a 30 m grid spacing adjacent to the surface and 43 levels located within 2 km of the ground. The simulation period is from 1 to 30 July 2012. Initial and boundary conditions for the meteorological variables were based on analyses from the National Center for Environmental Prediction's Global Forecasting System (GFS) model that uses a 1° grid spacing, while initial and boundary conditions for trace gases and aerosols were obtained from the global MOZART model [*Emmons et al.*, 2010] that uses a 2° grid
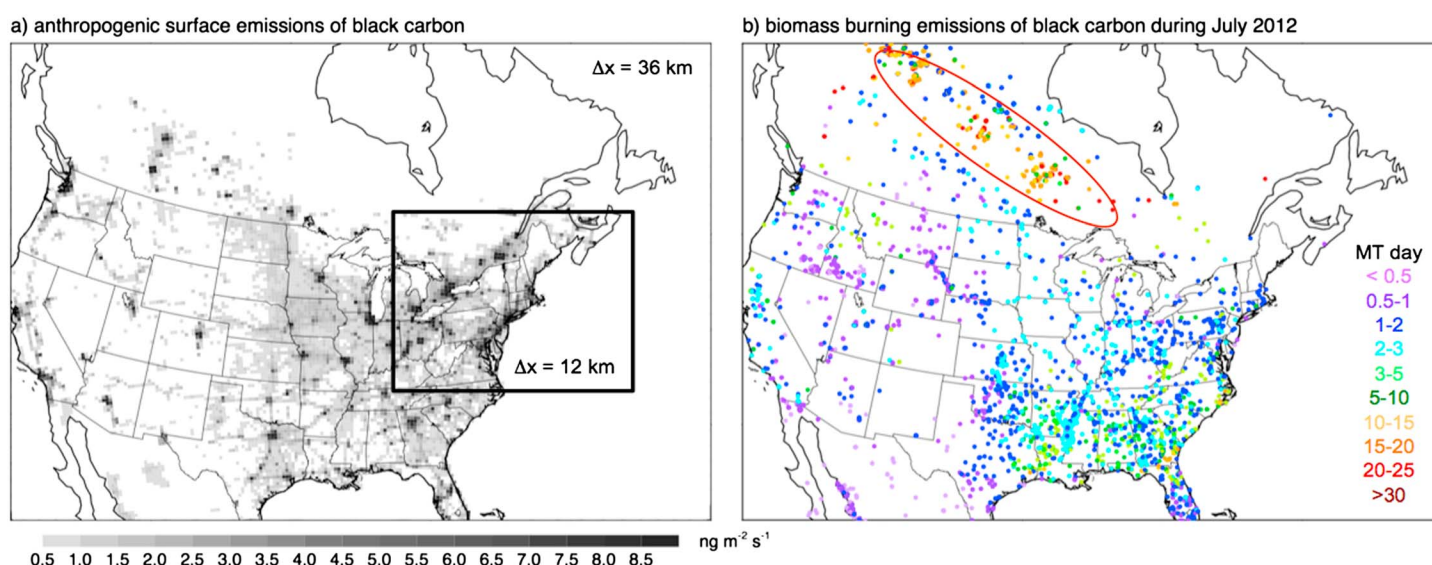
Figure 2. Outer nested domain used by WRF-Chem along with (a) the distribution of anthropogenic surface emissions of black carbon and (b) locations of all fires during July 2012 derived from satellite measurements. Black box in Figure 2a is the inner nested domain used by WRF-Chem and the red oval in Figure 2b denotes the fires with the highest emission rates.

spacing. This version of MOZART uses climatological distributions of dust (defined as other inorganics, OIN, in WRF-Chem) rather than online calculations of dust emissions; therefore, we reduced the dust concentrations by a factor of 2 as described by *Fast et al.* [2014] since the climatological dust concentrations could adversely affect simulated extinction in the free troposphere. Boundary conditions were updated at 6 h intervals from both models and then interpolated linearly in time by WRF-Chem. A series of overlapping 36 h simulations were performed in which the meteorological conditions were reinitialized at 00 UTC on each day using the GFS analysis. In contrast, the trace gas and aerosol species from the previous simulations were used as initial conditions. The first 12 h were used as spin-up periods and the series of concatenated 12–36 h forecasts were used in our analyses. Four-dimensional meteorological data assimilation was applied above 4 km agl using wind, temperature, and moisture analyses from the GFS model and a relaxation time scale of 6 h so that the simulated large-scale flows did not diverge from observed synoptic conditions.

The domain size was selected to include most of the emission sources in North America that could influence aerosols over the TCAP sampling domain. Aircraft sampling and much of the surface measurements did not start until 9 July; therefore, the simulation period from 1 to 9 July can be viewed as a spin-up period to produce realistic aerosol variations in the region.

Anthropogenic emissions of trace gases and aerosols were obtained from the National Emission Inventory 2011 (NEI 2011). This inventory contains hourly emissions for a representative weekday using a 4 km grid spacing over North America. The 4 km emission rates are aggregated to the larger 36 and 12 km grid spacing used by the two domains. An example of the distribution of black carbon emissions is also shown in Figure 2a. The emission inventory provides the total PM2.5 and PM10 mass emitted, but not the size distribution. Table S2 shows how the anthropogenic PM2.5 and PM10 emissions are distributed among the eight size bins used by MOSAIC that are based on an observed aerosol size distribution in the Houston metropolitan area [*Fast et al.*, 2006]. Emissions of semivolatile and intermediate volatility SOA trace gas precursors were assumed to be 6.5 times the mass of primary organic aerosol emissions from anthropogenic and biomass burning sources, as in *Shrivastava et al.* [2011] and *Tsimpidi et al.* [2010]. Biogenic emissions were computed online using the Model of Emissions of Gases and Aerosols from Nature (MEGAN) model [*Guenther et al.*, 2006] and lumped into isoprene, terpenes, and sesquiterpenes for the SAPRC-99 photochemical mechanism. Sea salt emissions (sodium and chloride) from the ocean were computed online using fluxes based on predicted surface winds and boundary layer quantities as described by *Gong et al.* [2002]. Dust emissions were obtained from GOCART scheme [*Ginoux et al.*, 2001; *Zhao et al.*, 2010] and occur primarily over the southwestern U.S. and northwestern Mexico. Dust in the MOSAIC model is lumped together with anthropogenic emissions of other inorganics.

Biomass burning emissions are based on the Fire INventory from NCAR (FINN) [*Wiedinmyer et al.*, 2011]. FINN uses satellite observations of active fires along with land cover, emission factors, and fuel loading to provide estimates of daily emission rates for trace gases and aerosols. To obtain hourly emission rates, we impose a diurnal variation to the fire emissions in which the highest and lowest emission rate occurs during the late afternoon and early morning, respectively, as in *Fast et al.* [2009]. The diurnal variation is similar to climatological values derived from GOES imagery shown in *Zhang et al.* [2012]. As shown by the black carbon emissions from fires during July in Figure 2b, the largest fires occurred in a band stretching from western Ontario to northern Alberta. There were fires with moderate emission rates located in the southeastern U.S.; however, preliminary tracer simulations using WRF-Chem indicated that the metrological conditions during July 2012 were not favorable to transport smoke from the southeastern U.S. into the TCAP sampling domain (not shown).

2.3. CAM5 Description

In this study the version 5.3 of the Community Atmosphere Model (CAM5) [*Neale et al.*, 2010] is also used to simulate the aerosol properties during TCAP. Model simulations are performed with the finite volume dynamical core at $1.25° \times 0.9°$ with 30 vertical layers. The time step for physical parameterizations is 30 min. The model is nudged toward ERA-Interim reanalysis winds [*Zhang et al.*, 2014] with a relaxation time scale of 6 h. Only the horizontal winds are nudged, because temperature nudging is found to have a negative impact on the simulated cloud and aerosol life cycle in CAM5 [*Kooperman et al.*, 2012; *Zhang et al.*, 2014; *Ma et al.*, 2015].

The three-mode version of the Modal Aerosol Model (MAM3) is used to represent aerosol populations in the Aitken, accumulation, and coarse mode [*Liu et al.*, 2012; *Ghan et al.*, 2012]. The simulated aerosol compositions considered are black carbon, primary and secondary organic aerosols, sulfate, sea salt, and dust. Sulfate is assumed to be in the form of ammonium sulfate; therefore, ammonium is a diagnosed quantity. As described by *Liu et al.* [2012], CAM5 includes a simple treatment of SOA formation that is based on fixed mass yields and a single semivolatile organic gas-phase specie that lumps isoprene, terpenes, toluene, as well as alkanes and alkenes with four or more carbon atoms (called BIGALK and BIGENE). Gas chemistry treats sulfur gases and H_2O_2, with oxidants prescribed by climatological values simulated by MOZART. The model uses a two-moment stratiform cloud microphysics parameterization [*Morrison and Gettelman*, 2008; *Gettelman et al.*, 2008, 2010]. Aerosols can act as cloud condensation nuclei and ice nucleating species (solution droplets or ice nuclei). The *Zhang and McFarlane* [1995] parameterization is used for deep convection, while the *Park and Bretherton* [2009] parameterization is used for shallow convection. The Rapid Radiative Transfer Model for General Circulation Models (RRTMG) is used to perform the shortwave and longwave radiative transfer calculations. More detailed information about the formulation of the default version of CAM5 can be found in *Neale et al.* [2010].

The model simulation started at 00 UTC on 1 May 2012. Initial concentrations of aerosols and their precursors were taken from a previous climatological simulation. Model output in the first 2 months is used as a spin-up period. Anthropogenic emissions for aerosols and their precursors over North America were obtained from NEI 2011 as in WRF-Chem simulations. However, daily mean values are used and the diurnal cycle is not considered. For other regions, the default CAM5 emissions for the year 2000 are used. As in the default version of CAM5, 2.5% of sulfur emissions are assumed to be primary sulfate aerosols and 97.5% of them to be SO_2. Since the vertical grid spacing in WRF-Chem is finer than CAM5, the height-dependent emissions (i.e., stack emissions) in WRF-Chem are added together within the coarser vertical layers in CAM5 so that the vertical distribution of emissions between the two models is similar. Aerosol emission size distributions are kept as close as possible to the default version of CAM5, rather than the size distribution used in WRF-Chem. Anthropogenic emissions above the lowest layer are set to those from energy/industry sectors. Emissions of the single SOA precursor gas involve fixed yields applied to emissions of isoprene, terpenes, toluene, BIGALK and BIGENE. Biogenic emissions for isoprene and terpene are prescribed from the MOZART-2 [*Horowitz et al.*, 2003] data set as in default version of CAM5 [*Neale et al.*, 2010]. Sea salt and dust emissions are computed online and depend on the predicted surface wind speeds. As in WRF-Chem, biomass burning emissions are based on FINN, but the diurnal cycle is not considered and daily mean emissions are used instead. Daily means are usually the highest temporal resolution of biomass burning emissions used by hindcast global climate modeling studies (e.g., AeroCom phase III biomass burning experiments, https://wiki.met.no/_media/aerocom/aerocom_bbexperiment_proposed_v3.2.pdf).
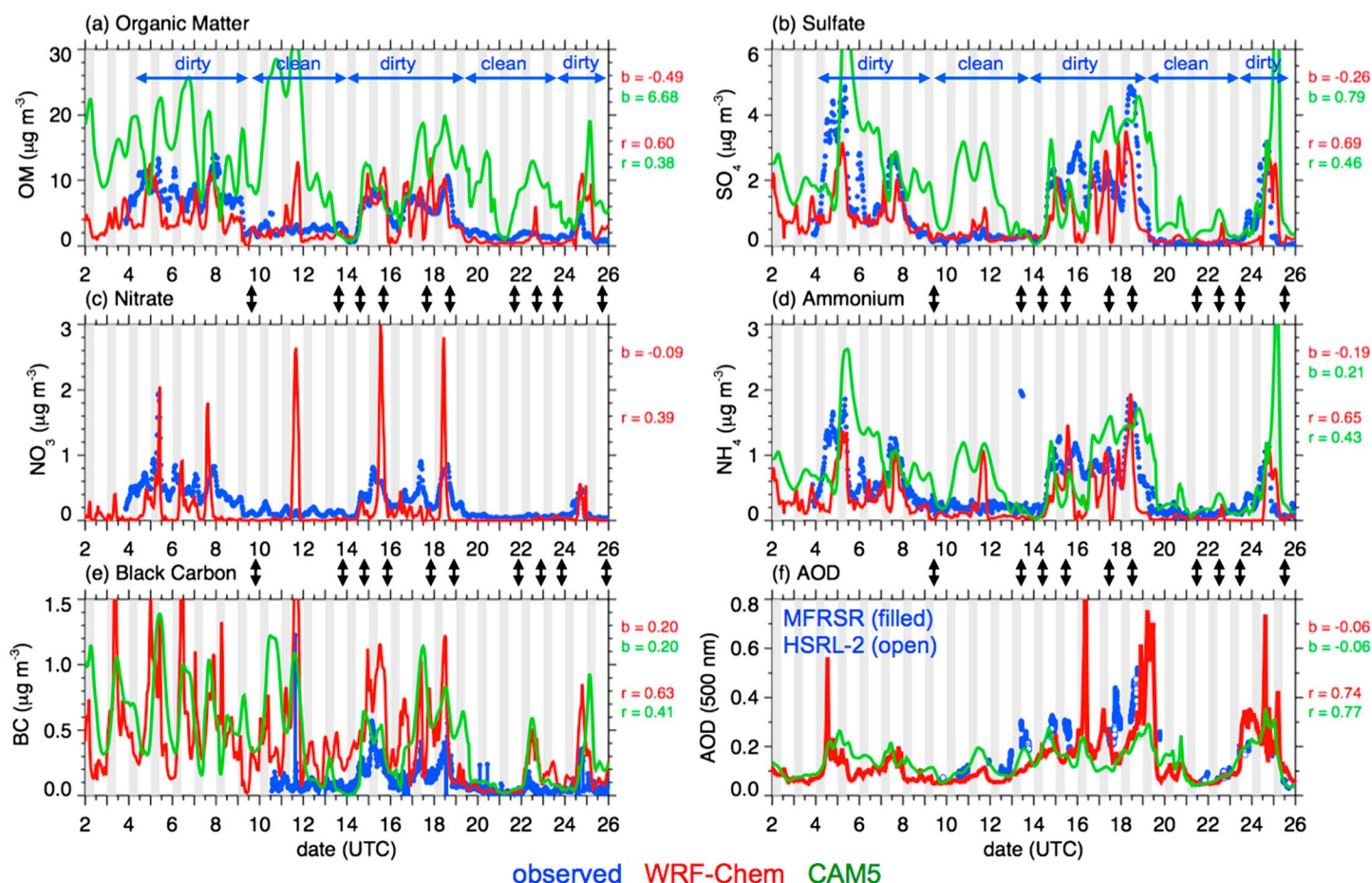
Figure 3. Observed (blue) and simulated (a) organic matter, (b) sulfate, (c) nitrate, (d) ammonium, (e) black carbon, and (f) AOD from WRF-Chem (red) and CAM5 (green) at the Cape Cod AMF site during July 2012. The black arrows denote the aircraft flight periods, b is the bias, and r is the correlation coefficient.

3. Results

Given that the spatial resolution of WRF-Chem, CAM5, and the observations are different, the supporting information provides details on how the models are compared with the TCAP measurements.

3.1. Overall Temporal and Vertical Variations During the TCAP

The variability in observed and simulated aerosol composition ($<1\,\mu m$) and AOD (at 500 nm) over the AMF during July 2012 is summarized in Figure 3. The observed temporal variability of organic matter (OM), sulfate (SO_4), nitrate (NO_3), ammonium (NH_4), and black carbon (BC) indicate distinct periods of high and low concentrations denoted by "dirty" and "clean," respectively. The higher concentrations of these species occur during periods of near-surface and midtropospheric southwesterly to northwesterly winds (Figure S1) which are favorable for transport from anthropogenic emission sources, especially those along the entire northeast urban corridor. Aerosol concentrations are lower during periods of southeasterly to northeasterly near-surface winds (Figure S1) that transport relatively cleaner air over the ocean toward Cape Cod. The multiday temporal variations produced by WRF-Chem are similar to the observations; however, the model sometimes produces low aerosol concentrations for several hours during the dirty periods when the observations remain relatively high for several days. A somewhat poorer representation of the multiday temporal variability was produced by CAM5, since it often produces high aerosol concentrations even during the clean periods. The correlation coefficient from WRF-Chem ranges from 0.60 to 0.69 for OM, SO_4, NH_4, and BC, while those from CAM5 range from 0.38 to 0.46 (Table 1). The average observed OM between 9 and 30 July comprises ~68% of the total PM1 (Figure S2), compared to 72% from WRF-Chem and 80% from CAM5. In WRF-Chem, 69, 18, and 13% of OM originate from anthropogenic, biogenic, and biomass burning sources, respectively.

Table 1. Statistics for PM1, Defined as the Sum of OM, SO_4, NO_3, NH_4, and BC, at the AMF Site in Terms of Bias and Correlation Coefficient, R[a]

		PM1	OM	SO_4	NO_3	NH_4	BC	AOD
Observed	Mean	5.53	3.86	0.91	0.23	0.43	0.10	0.170
WRF-Chem		4.70	3.37	0.65	0.14	0.24	0.30	0.108
WRF-Chem no KF-Cup	Mean	4.77	3.45	0.63	0.15	0.24	0.30	0.124
CAM5		13.18	10.54	1.70	-	0.64	0.30	0.113
WRF-Chem		−0.83	−0.49	−0.26	−0.09	−0.19	0.20	−0.062
WRF-Chem no KF-Cup	Bias	−0.76	−0.41	−0.28	−0.08	−0.19	0.20	−0.046
CAM5		7.65	6.68	0.79	-	0.21	0.20	−0.057
WRF-Chem		0.64	0.60	0.69	0.39	0.65	0.63	0.74
WRF-Chem no KF-Cup	R	0.64	0.58	0.68	0.40	0.65	0.63	0.77
CAM5		0.32	0.38	0.46	-	0.43	0.41	0.77

[a]Observed PM1 obtained from the ACSM and SP2 instruments.

The high concentrations from CAM5 are likely due to the high SOA yield applied at the surface and the coarse resolution (Figure 1) in which Boston emissions are spread over a wide region that includes Cape Cod Bay and the AMF site. While simulated BC is somewhat correlated with the SP2 data (correlation coefficients of 0.63 and 0.41 for WRF-Chem and CAM5, respectively), both models have a positive bias in BC concentrations (Figure 3e) that are ~2.8 times higher than the observed average of $0.10\,\mu m\,m^{-3}$ between 10 and 25 July despite the differences in meteorological circulations and emission rates associated with spatial resolution.

An evaluation of simulated AOD at 500 nm is shown in Figure 3f. Observed AOD was obtained from both the MFRSR instrument at the AMF site as well as from the HSRL-2 when it flew directly over the AMF site. *Ortega et al.* [2016] also derived AOD from a 2-Dimensional Multi Axis Differential Optical Absorption Spectroscopy (2D-MAX-DOAS) instrument [*Coburn et al.*, 2011; *Ortega et al.*, 2015] and found that it differed from the MFRSR values by −0.012 on average. While the AOT from HSRL-2 extends only up to 7.5 km, it should encompass a large fraction of the aerosols in the atmosphere. In fact, there is very good agreement between the two measurements. Note that the observed AOD from the MFRSR is available only during daytime under mostly clear skies. Unfortunately, circus clouds frequently occurred over the AMF site so that AOD could not be derived for a large fraction of daytime hours during TCAP. The multiday variation in the observed AOD is similar to the variations in surface aerosol concentrations associated with the dirty and clean periods, but upon closer inspection the shorter time scale variations in observed AOD are not necessarily correlated with changes in surface aerosol concentrations (Figure S3). This indicates that AOD during TCAP also depends on aerosol concentrations aloft. The simulated AOD from both models is similar to the observed with a correlation coefficient of 0.74 from CAM5 and 0.77 from WRF-Chem and a bias from both models of about −0.06. However, WRF-Chem produces significantly higher AOD than CAM5 for short time periods. Since the AOD from CAM5 is too low, the simulated aerosol concentrations aloft should be lower than observed to offset the positive bias in the near-surface concentrations.

The concentration and temporal variability of trace gases simulated by WRF-Chem at the AMF site are also in reasonable agreement with the available measurements of O_3, NO, NO_2, CO, SO_2, and glyoxal (Figure S4). As with BC, (Figure 3e) simulated CO during the dirty periods is usually higher than observed. Since CO and BC are emitted primarily from vehicles, the NEI 2011 estimates may be too high. In contrast, simulated NO is usually too low. Note that NO has a short lifetime so that NO measured at this site is likely due to emissions from U.S. Route 6 (about 2 km west of the AMF site), the main highway along the peninsula. Thus, the underprediction in simulated NO is likely due to the 12 km grid spacing that instantly dilutes the narrow line of vehicle emissions in addition to other uncertainties in volatile organic compounds (VOCs) that affect the NO_x and HO_x cycles.

To examine variations of aerosols above the AMF site, profiles of simulated PM2.5 concentrations from WRF-Chem and CAM5 are shown in Figure 4. The temporal variations in PM2.5 concentrations aloft from WRF-Chem are overall similar to the alternating dirty and clean periods as defined by the surface measurements. However, the highest simulated PM2.5 is not always located close to the surface and there are many instances of aerosol layers passing over the AMF site during the month. Not surprisingly, the temporal variations and vertical gradients in PM2.5 concentrations aloft from CAM5 are smoother than those from WRF-Chem and it
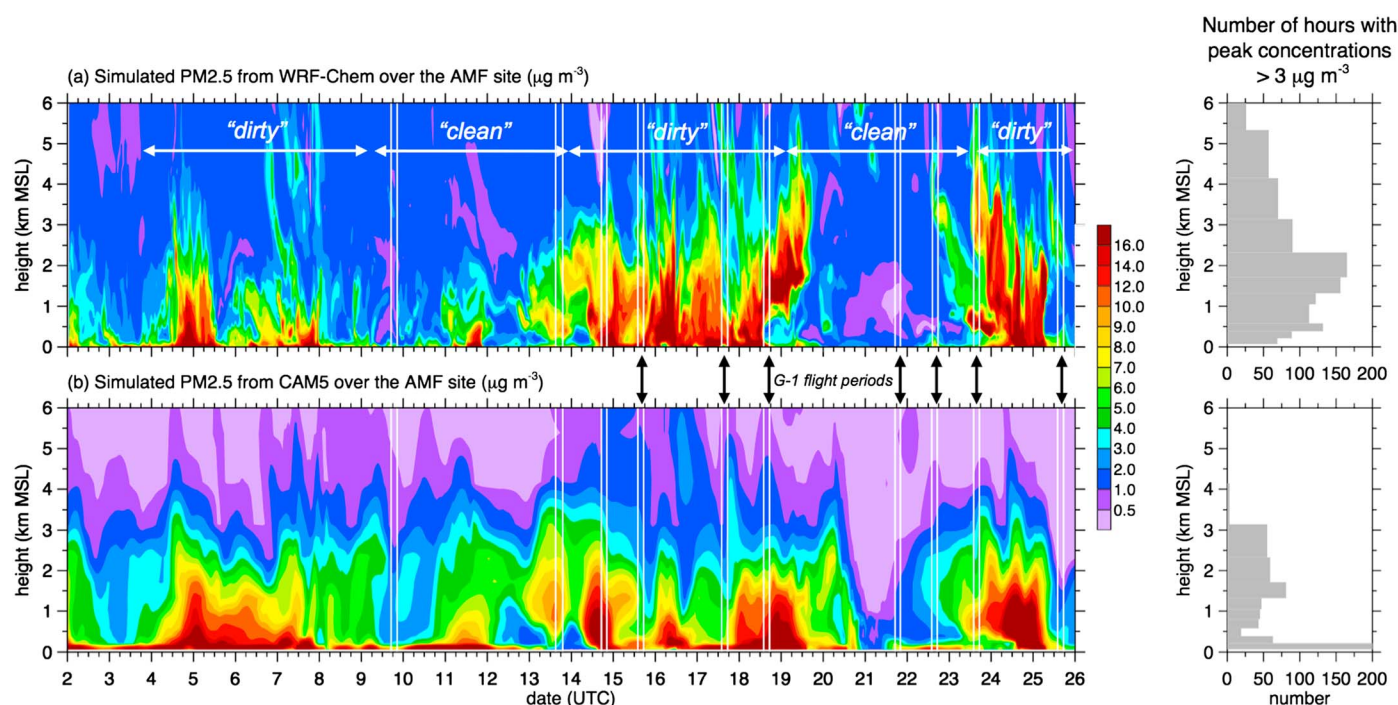
Figure 4. Profiles of simulated PM2.5 from (a) WRF-Chem and (b) CAM5 during July 2012 over the Cape Cod AMF site. The WRF-Chem profiles are within a 12×12 km grid cell, while the CAM5 profiles are within a $1.25° \times 0.9°$ grid cell as depicted in Figure 1. Black arrows and white vertical lines denote the aircraft flight periods. Gray shading in the right panels denote number hours of local maxima (aerosol layers) with peak concentrations $>3 \mu g\,m^{-3}$ between 2 and 26 where both models use CAM5's vertical grid spacing to compute the frequency as a function of altitude.

is difficult to identify the same dirty and clean periods. While CAM5 also produces aerosol layers aloft, there are far fewer of them than from WRF-Chem. About twice as many layers can be identified between 1 and 3 km from WRF-Chem than from CAM5 (right panels of Figure 4). Most of the PM2.5 mass from CAM5 is also located within 3 to 4 km of the surface, but aerosol concentrations from WRF-Chem above this altitude often exceed $3 \mu g\,m^{-3}$ and there are 50 to 100 h in which layers that can be identified (9 to 17% of the simulation period).

As at the surface, most of the OM aloft from WRF-Chem at the AMF site is from anthropogenic sources as shown in Figures 5 and S5. On average, about 50, 30, and 10% of the OM below 2 km is from anthropogenic, biogenic, and biomass burning sources, respectively (Figure 5a). The remaining 10% of the OM originates from the MOZART boundary conditions and this fraction increases with height and becomes as large as 60% of the total OM above 5 km. While this fraction is large in the middle and upper troposphere, the total OM concentrations are small. Figure S5 shows that the simulated fraction of organic aerosols from various sources varies substantially during the month, with higher fractions of biogenic OM prior to July 16 and higher fractions of biomass burning OM after 19 July. Regional-scale circulations below 3 km prior to 16 July were favorable for transport from the southwest where there are sources of biogenic precursor emissions. Northwesterly to northeasterly winds became more frequent after 19 July (Figure S1), so that transport is less favorable from biogenic source and more favorably for transport from biomass burning sources in Canada. For the G-1 flights during clean periods over the AMF site on 9, 21, 22, and 25 July (Figure 5b), the simulated average OM concentrations are usually less than $1 \mu g\,m^{-3}$ but the fraction of biomass burning OM becomes as high as 40% and the fraction of anthropogenic OM decreases to 10–20% below 3 km. The relatively higher biomass burning OM at this time is largely due to one large plume transported over the AMF site on 25 July (Figure S5). During the dirty period G-1 flights on 13–15, 17, 18, and 23 July (Figure 5 c), the simulated fraction of anthropogenic OM is as high 60–70% below 3 km.

The miniSPLAT measurements were divided into 11 composition classes including biomass burning aerosols, as described by *Zelenyuk et al.* [2015]. Biomass burning aerosols from miniSPLAT are from primary emissions plus condensed SOA from biomass burning VOCs. Figures 5d and 5e show the volume associated with biomass burning aerosols along with the simulated values. Biomass burning aerosols from WRF-Chem are
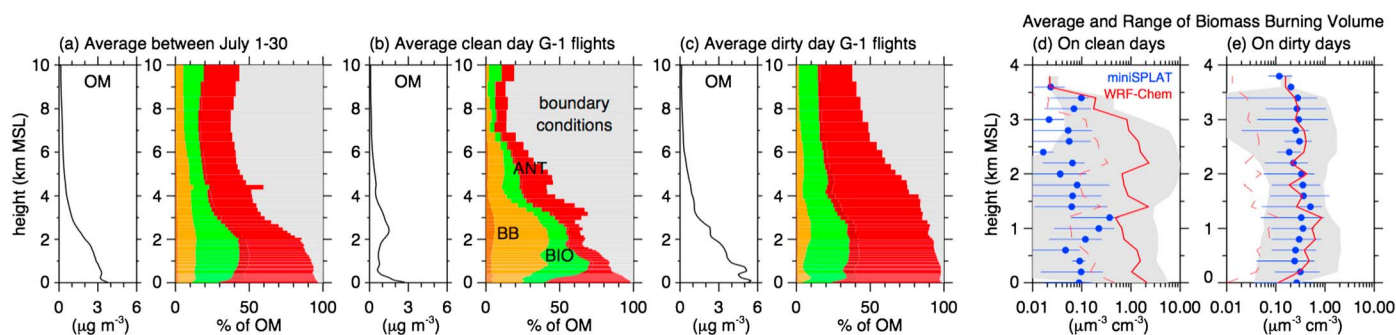
Figure 5. Simulated OM profiles and fraction of OM from anthropogenic (ANT), biogenic (BIO), biomass burning (BB), and boundary condition sources over the AMF site from WRF-Chem averaged over the (a) entire simulation period, (b) G-1 flights on "clean" days, and (c) G-1 flight periods on "dirty" days. Dark and light shading for biomass burning and anthropogenic OM sources represent primary and secondary aerosols, respectively. The observed and simulated profiles of volume from biomass burning sources in the Cape Cod Column averaged over the (d) G-1 flights on "clean" days and (e) G-1 flights on "dirty days". Solid red line and gray shading in Figures 5d and 5e represent average and range of simulated values, respectively, of primary and secondary biomass burning, while dashed red line is primary biomass burning aerosols.

from both primary and secondary OM. During the clean G-1 flights, the simulated biomass burning OM volume is higher than observed by as much as an order of magnitude on average (Figure 5d). In contrast, the simulated biomass burning OM volume is similar to observed at all altitudes on the dirty G-1 flight days (Figure 5e). Since the average observed fractions of biomass burning aerosol from miniSPLAT are similar among all the G-1 flights and did not have significant differences between the clean and dirty periods, the model produced much more variability in the fraction of biomass burning aerosols than observed. The observed average percentage of PM1 number and volume of biomass burning particles from miniSPLAT for each flight along with the simulated values are listed in Table 3. The observed percentage of PM1 that were identified as biomass burning particles ranged from 3.8 to 11.3% in the Cape Cod Column and 4.4 to 7.8% in the Maritime Column. These results suggest that the smoke plumes from the large Canadian fires are sufficiently diluted by the time they arrive over Cape Cod and/or the biomass burning particles originated from other smaller fires closer to Cape Cod. Simulated secondary biomass burning concentrations are about an order of magnitude larger than those due to primary emissions. The simulated total biomass burning percentages and volume are lower than observed on 9 and 13–5 July, close to observed on 17 and 18 July, and higher than observed for the remaining flights. The simulated outlier on 25 July when the model predicts nearly half of the aerosol concentrations are smoke when the miniSPLAT data suggests that less than 5% of the particles are smoke.

Some of the simulated aerosol layers aloft occurred during the 10 aircraft sampling periods as shown by the arrows in Figure 4. We now use the profiles of extinction from the HSRL-2 to evaluate the simulated AOT in two layers: the residual layer and the free troposphere. One advantage of TCAP measurement is that the HSRL-2 profiles of extinction provide a means of evaluating the vertical distribution of aerosols aloft that cannot be obtained from column values from surface or satellite column-integrated measurements. In our analysis of the HSRL-2 data, we first adopt the same definitions for these layers as in *Berg et al.* [2016] for six aircraft sampling periods as shown in Figure 6 in which the boundary between the residual layer top and the free troposphere ranged from 2.65 to 2.93 km. The gross vertical variations in simulated extinction WRF-Chem are qualitatively similar to the HSRL-2 measurements in that the fraction of AOT in the free troposphere on 21 and 22 July was the highest and on 13 July was the lowest. Over the Cape Cod column the observed fraction of AOT in the free troposphere was between 50 and 65%, but the simulated values from WRF-Chem were somewhat higher between 65 and 85%. Similarly on 13 July, the simulated fraction of AOT in the free troposphere was higher than observed. On 15, 17, and 25 July, the simulated values were closer to the observations. In contrast, the fraction of AOT in the free troposphere from CAM5 bears little resemblance to the HSRL-2 observations and has a much smaller amount of variability. Most of the fraction of AOT in the free troposphere is less than 40%, consistent with the vertical distribution of PM2.5 shown in Figure 4b.

A more detailed evaluation of the vertical variation in simulated extinction is shown in Figure 7 by using percentiles that include data from multiple flights separated into clean and dirty periods. Because the vertical grid spacing in the models are larger than the 15 m range gates from HSRL-2, percentiles are computed
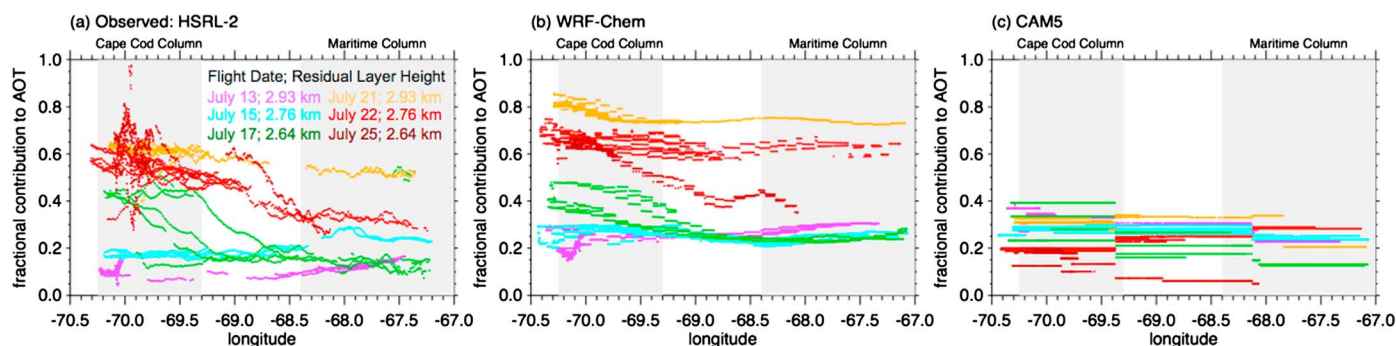
Figure 6. Spatial variations in fraction of AOT (up to 9 km MSL) in the free troposphere (a) observed by HSRL-2 and simulated by (b) WRF-Chem and (c) CAM5 on 13, 15, 17, 21, 22 and 25 July. The assumed boundary between the residual layer and free troposphere for each flight is given in Figure 6a.

within 0.25 km for layers up to 5 km msl followed by 0.5 km for layers above 5 km. Extinction from WRF-Chem is binned into these layers, but extinction from CAM5 is binned into fewer layers because of its coarser vertical grid spacing. Note that 2 days have been split into both clean and dirty. Strong gradients in aerosol concentrations were observed in the region on 9 and 25 July, with low extinction over Cape Cod and higher extinction over the ocean. On 14 July, percentiles were only computed for the Cape Cod column because clouds obscured the HSRL-2 sampling over the ocean. There were also clouds on 13 July, but they were broken so that data were available to include in the percentiles for both columns. During the clean sampling periods (Figures 7a and 7b), stronger vertical variations in the observed extinction occurred over the Maritime Column with a distinct layer in the free troposphere between 3 and 4 km. Extinction from both WRF-Chem and CAM5 is generally lower than observed except for portions of the profiles. WRF-Chem produces values closer to observed between 2 and 3.5 km within the Cape Cod Column, while CAM5 produces values closer to those observed between 0.25 and 2 km. Within the Maritime Column, WRF-Chem produces extinction similar to observed for the layer in the free troposphere between 3 and 4 km but CAM5 produces values closer to observations within the residual layer below 2 km. Both models produce higher extinction during the dirty periods consistent with the HSRL-2 data (Figures 7c and 7d), with most of the extinction located within the residual layer below 3 km. Lumping all the aircraft data for the dirty periods hides some of the vertical variability in the free troposphere that will be examined later. The CAM5 extinction shows surprising variability (i.e., the 5th to 95th percentile range is often large), that is, due to variations over time, given the coarse horizontal grid spacing with up to two grid cells encompassing either the Cape Cod or Maritime Columns. WRF-Chem with its higher horizontal resolution does produce a larger range of extinction at many altitudes that are similar to observed (1.75 to 3.75 km in Figure 7a, 3 to 3.75 km in Figure 7b, and 0 to 2 km in Figure 7d) and at a few altitudes produces more variability than observed; however, the variability is still less than observed for a large fraction of the profiles in each column.

Statistics describing the performance of WRF-Chem and CAM in simulating the average PM1, defined as the sum of OM, SO$_4$, NO$_3$, NH$_4$, and BC, for each of the 10 G-1 flights is given in Table 2. Additional statistics describing the performance for the individual aerosol components are given in Tables S3–S7. Simulated PM1 from WRF-Chem is lower than observations from the AMS and SP2 instruments for six of the 10 flights, with correlation coefficients ranging from 0.07 on 25 July to 0.76 on 17 July. In terms of the largest biases, the simulated concentration is 3.2 and 2.8 times lower than observed on 9 and 21 July, respectively, and 1.75 times higher than observed on 17 July. In contrast, the average PM1 from CAM5 is higher than observed for nine of the 10 flights, ranging from 1.2 to 1.9 times higher than observed, and correlation coefficients ranged from 0.36 on 25 July to 0.72 on 17 July. For WRF-Chem, the low bias in PM1 is consistent with the overall low values of extinction shown in Figure 7. While the higher PM1 produced by CAM5 does lead to higher extinction than WRF-Chem at many altitudes (Figure 7), the overall extinction is still lower than observed. We note that the biases in PM1 concentrations are not exactly correlated with errors in the simulated extinction shown in Figure 7, since extinction also depends on coarser particles and aerosol water as will be discussed later for two flights.

We have shown that both models have some skill in simulating temporal and vertical variations in aerosols over the TCAP region; however, the simulations are far from perfect. We next examine two cases, 17 and
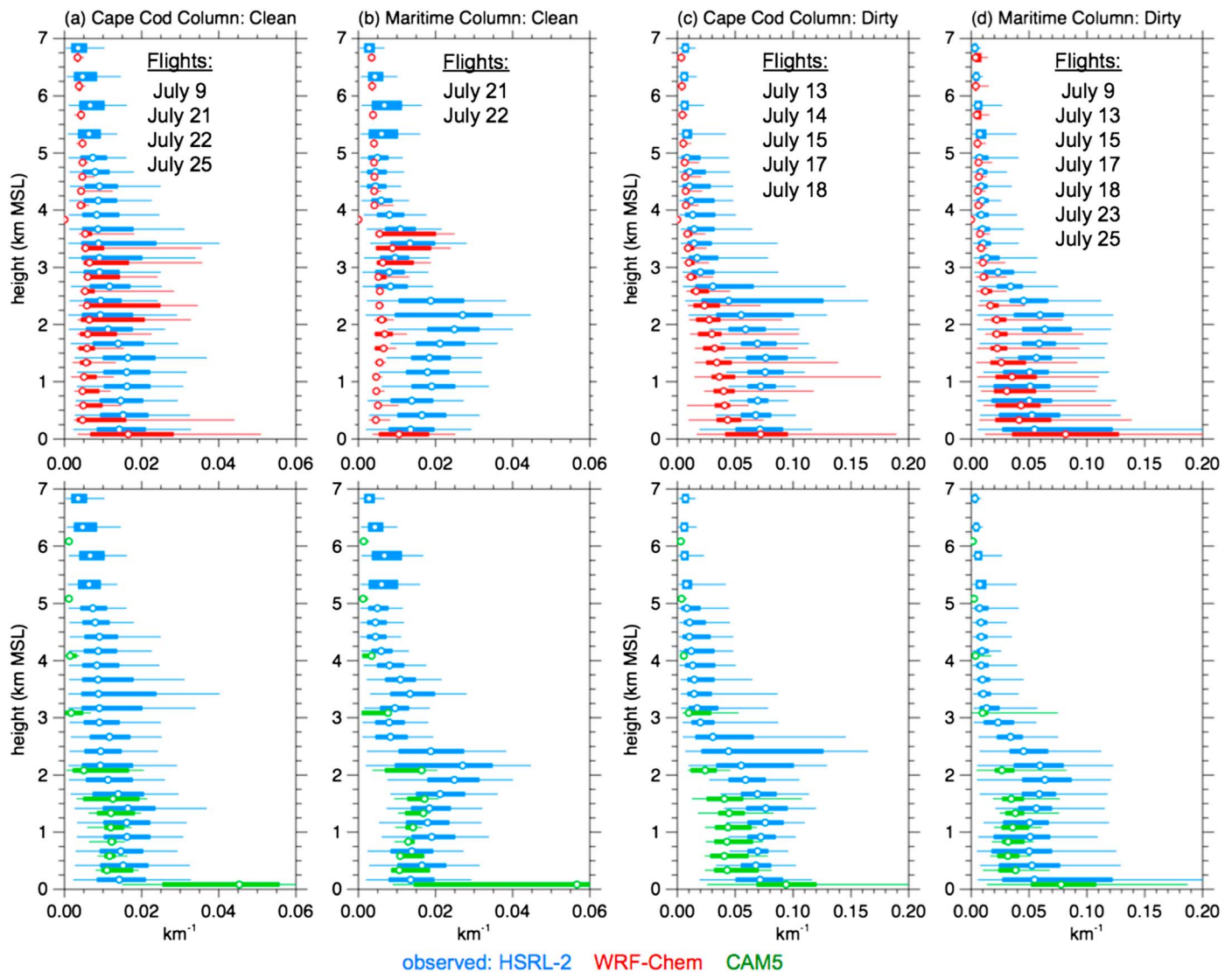
Figure 7. Vertical profiles of observed (blue) and simulated extinction from WRF-Chem (red) and CAM5 (green) during the "clean" (left two panels) and "dirty" (right two panels) periods. (a and c) Profiles within the Cape Cod Column; (b and d) profiles within the Maritime Column. The dots are the median, the horizontal bars are the 25th to 75th percentiles, and the horizontal lines are the 5th to 95th percentiles.

22 July, in more detail to better understand model performance and the processes that contribute to aerosol layers that may not be represented adequately in the models. For reference, aerosol layers on the other flights are illustrated in Figures S6–S13 that depict a portion of the longitudinal variation in observed and simulated extinction profiles and AOT.

3.2. Layering During the 17 July Dirty Period

The ambient winds over the AMF site on 17 July were westerly to northwesterly (Figure S1) and the aircraft flight paths were selected to be along the wind direction on that day (Figure 1). A deep layer of aerosols, denoted as the residual layer, was observed by the HSRL-2 (Figure 8a) that was ~2 km deep over Cape Cod that gradually increased to ~3 km over the ocean, ~230 km southeast of Cape Cod. For clarity, Figure 8 depicts a subset of the extinction profiles between 1521 and 1615 UTC during the aircraft sampling period between 1400 and 1720 UTC. Convective boundary layer processes over land are responsible for the residual layer. During the day as the convective boundary grows to a few kilometers in depth, aerosols are mixed from the surface up to the boundary layer top by turbulent eddies. The ambient winds subsequently transport this

Table 2. Statistics for PM1, Defined as the Sum of OM, SO$_4$, NO$_3$, NH$_4$, and BC, for Each of the G-1 Flights in Terms of Bias and Correlation Coefficient, R[a]

		Flight Day in July									
		9	13	14	15	17	18	21	22	23	25
Observed	Mean	3.56	6.62	7.81	8.19	4.31	7.81	2.02	2.48	2.97	1.23
WRF-Chem		1.10	6.32	8.04	7.08	7.53	5.21	0.71	2.04	3.81	2.41
WRF-Chem No KF-Cup	Mean	1.08	7.17	8.64	7.47	8.47	5.90	0.66	2.10	3.79	2.35
CAM5		5.91	7.85	13.11	6.16	6.94	9.16	3.84	3.77	5.28	3.59
WRF-Chem		−2.47	−0.30	0.23	−1.11	3.23	−2.60	−1.31	−0.44	0.84	1.17
WRF-Chem No KF-Cup	Bias	−2.48	0.55	0.83	−0.72	4.16	−1.90	−1.37	−0.37	0.81	1.12
CAM5		2.35	1.23	5.31	−2.03	2.63	1.35	1.82	1.30	2.30	2.36
WRF-Chem		0.57	0.34	0.70	0.65	0.76	0.19	0.33	0.12	0.41	0.07
WRF-Chem No KF-Cup	R	0.48	0.39	0.69	0.64	0.74	0.14	0.19	0.08	0.40	0.05
CAM5		0.53	0.60	0.62	0.68	0.72	0.63	0.58	0.20	0.53	0.36

[a]Observed PM1 obtained from the HR-ToF-AMS and SP2 instruments.

layer over the ocean that is largely decoupled from the stable marine boundary layer that is only on a few hundred meters deep due to the relatively cool ocean temperature. At this time, the highest values of extinction were observed in the Maritime Column, although there are also large horizontal and vertical variations within the column. Another aerosol layer in the free troposphere between 3 and 5 km was observed over the AMF site. This layer was not observed shortly after 14 UTC at the beginning of the flight, but was present when the King Air made its second pass back over the AMF site between 1520 and 1540 UTC [*Berg et al.*, 2016]. By 17 UTC, higher values of extinction occurred in this layer; it was transported farther to the east (not shown). Since the HSRL-2 flew back and forth along the same path, it was able to observe the progression of these layers as they were transported toward the east and direct the G-1 aircraft to sample layers in both the Cape Cod and Maritime Columns.

The extinction profiles simulated by WRF-Chem and CAM5 for the same period are shown in Figures 8b and 8c, respectively. While both models qualitatively represent the horizontal variations in extinction profiles associated with residual layer as well as the presence of a layer in the free troposphere, there are important differences with the HSRL-2 extinction profiles. For WRF-Chem (Figure 8b), the residual layer is shallower than observed in the Cape Cod Column, and the peak values in the free troposphere aerosol layer are located ~1 km higher than observed. While the simulated extinction between 4 and 5.5 km msl is similar to observations, the model misses the higher values seen in the observations between 3 and 4 km msl. The model produces some variability in the highest extinction above the ocean surface in the Maritime Column, but it does not completely resemble the complexity seen in the HSRL-2 data. The free troposphere layer also arrives earlier than observed so that extinction of 0.01 to 0.02 km^{-1} was produced east of 69°W. In contrast, the HSRL-2 measurements show very low extinction in the free troposphere east of 69°W. For CAM5 (Figure 8c), the residual layer is also shallower than observed over the Cape Cod Column. The CAM5 extinction in residual layer is also about a factor of 2 lower than observed and that from the WRF-Chem simulation. In contrast to WRF-Chem,
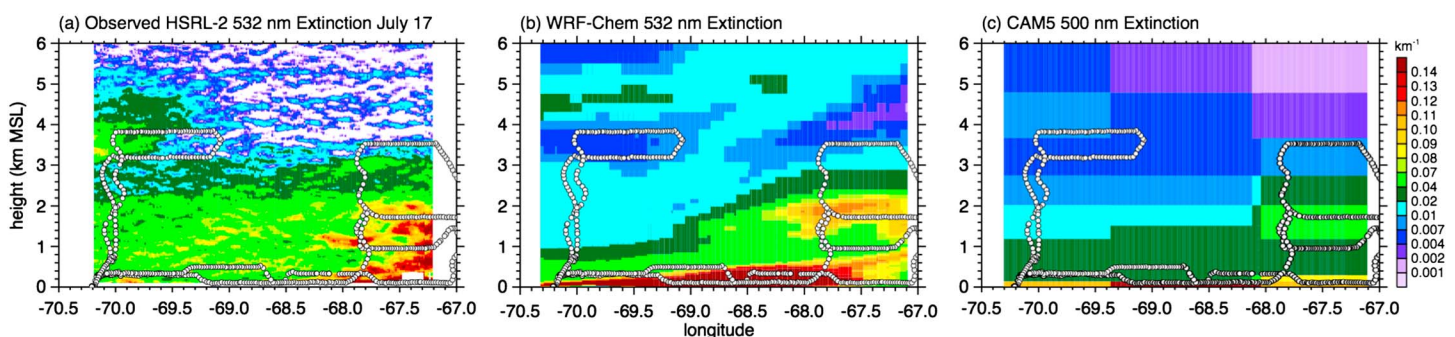
Figure 8. Extinction profiles on 17 July as a function of longitude between 1521 and 1615 UTC (a) observed by HSRL-2 and (b) simulated by WRF-Chem and (c) CAM5. The dots denote the sampling altitude of the G-1 aircraft during the entire flight.
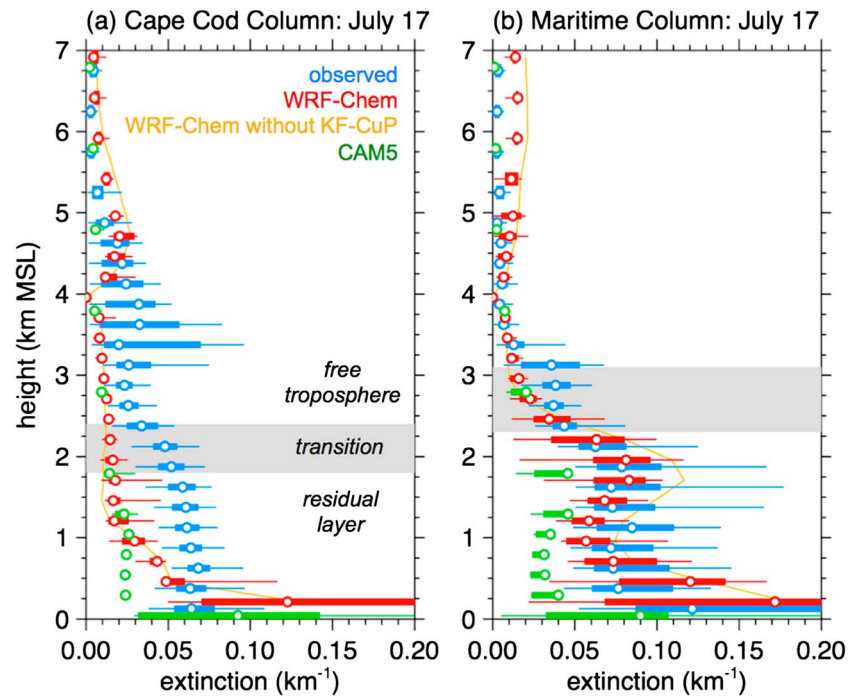
Figure 9. Vertical profiles of observed (blue) and simulated extinction from WRF-Chem (red) and CAM5 (green) in the (a) Cape Cod Column and (b) Maritime Column on 17 July. The dots are the median, the horizontal bars are the 25th to 75th percentiles, and the horizontal lines are the 5th to 95th percentiles. The orange line is from the WRF-Chem simulation without the effect of KF-CuP on aerosols.

CAM5 produces a weak layer in the free troposphere over the Cape Cod column that arrives about the same time as observed by HSRL-2 so that the low values of extinction are found east of 69°W. The layer over Cape Cod is located at a somewhat higher altitude than observed similar to WRF-Chem, but one needs to keep in mind that the vertical grid spacing used in CAM5 at this altitude is coarse (~1 km).

Using percentiles in a manner similar to Figure 7, a quantitative assessment of the simulated extinction profiles over the entire flight period for the Cape Cod and Maritime Columns is shown in Figure 9. The transition zone between the residual layer and the free troposphere denoted by gray shading is based on vertical profiles of potential temperature (θ) and relative humidity (RH) from G-1 aircraft observations (Figures 10g and 10h) as well as profiles of extinction. The largest variability in the Cape Cod column is produced between 3 and 5 km, associated with the passage of the aerosol layer aloft (Figure 9a). The extinction profiles also indicate that the observed depth of the residual layer is between 2 and 2.5 km during the aircraft flight. Simulated extinction from both models is generally lower than observed, except very close to the surface where the extinction is too high. In the free troposphere portion of the Cape Cod Column, the WRF-Chem median extinction of 0.02 km^{-1} at 4.75 km msl is somewhat lower than the peak median of 0.03 km^{-1} observed at 3.75 km msl. The simulated range of extinction for that layer is also far lower than observed. While CAM5 does produce an aerosol layer in the free troposphere (Figure 8c), the increase in extinction is very small, so that it is difficult to see the increase using the linear scale shown in the figure. In the Maritime Column (Figure 9b), the median and range of extinction from WRF-Chem is very similar to measured values throughout most of the residual layer while the median from CAM5 is about a factor of 2 too low. While the residual layer in WRF-Chem is consistent with HSRL-2 between 1521 and 1615 UTC (Figure 8b), it is shallower than observed for the entire flight period (1400 and 1720 UTC) as indicated by the low extinction between 2.5 and 3.25 km msl. In the free troposphere east of 69°W, the extinction from WRF-Chem is higher than observed while the extinction from CAM5 is close to observed.

The profiles of in situ measurements from the HR-ToF-AMS and SP2 instruments along with profiles of θ and RH are shown in Figure 10 to illustrate the association between the meteorological and extinction profiles. We compute percentile profiles for each aerosol component within 50 m bins up to the highest altitude flown
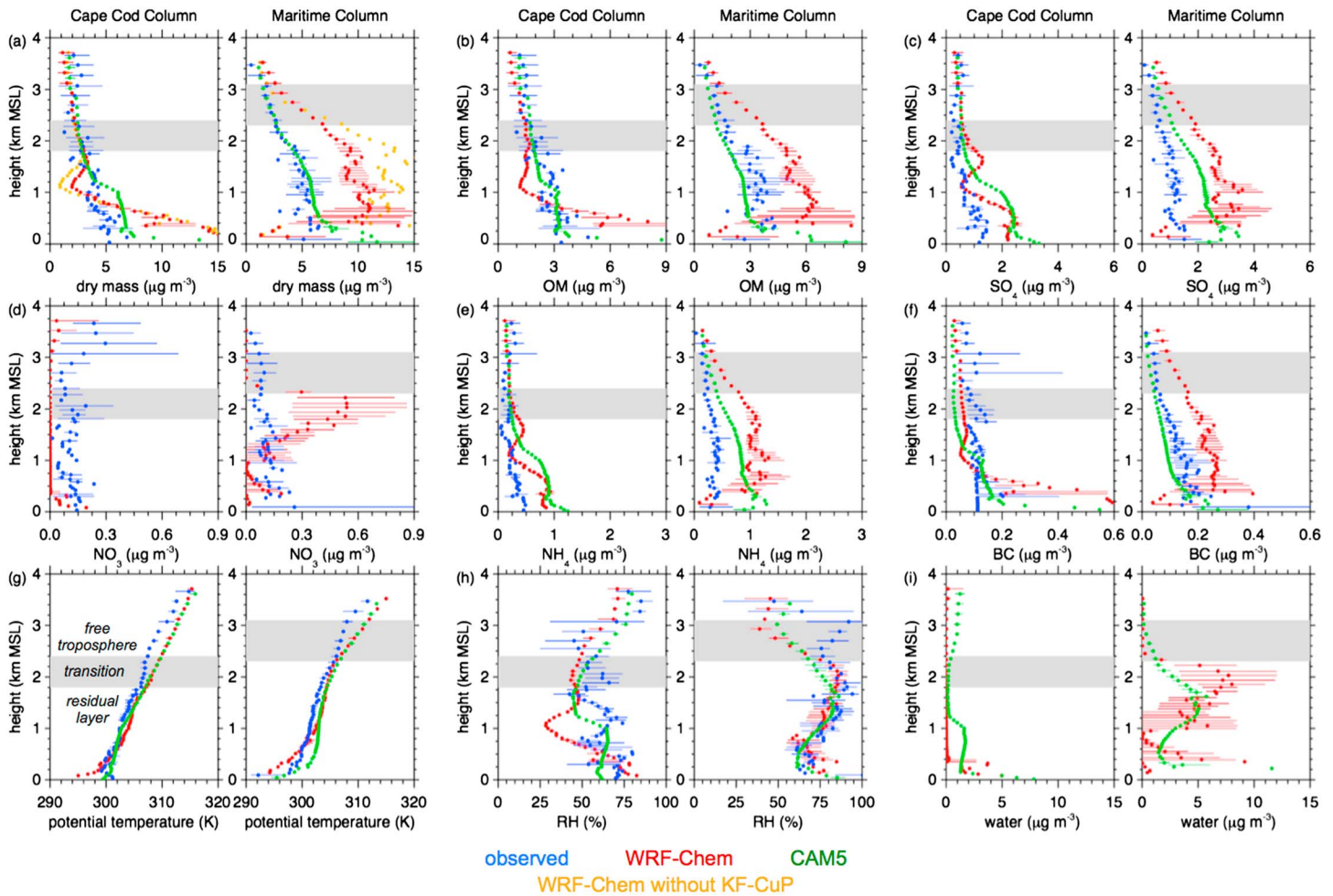
Figure 10. Observed and simulated profiles of (a) PM1 mass, (b) organic matter, (c) sulfate, (d) nitrate, (e) ammonium, (f) black carbon, (g) potential temperature, θ, (h) relative humidity, RH, and (i) aerosol water for the G-1 flight on 17 July. Dots and horizontal lines denote the average and range, respectively, at each altitude. Only PM1 is shown for the WRF-Chem simulation without KF-CuP. Nitrate is not simulated by CAM5.

by the G-1 aircraft that is about 3.75 km on this day. In general, the horizontal and vertical variations in measured dry PM1 mass (mass of particles with diameters less than 1 μm), defined here as the sum of OM, SO_4, NO_3, NH_4, and BC (from HR-ToF-AMS and SP2 instruments), is consistent with the variations in the extinction measured by HSRL-2. For example, higher and lower PM1 is observed in the residual layer and free troposphere, respectively. In addition, the G-1 indicates large vertical gradients in PM1 with higher concentrations in the lower half of the residual layer similar to the extinction profiles. In terms of horizontal gradients, PM1 in the Maritime Column were usually between 4 and 7 μg m^{-3} while the concentrations were somewhat lower and usually between 3 and 6 μg m^{-3} in the Cape Cod column. While there are somewhat higher values of PM1 in the Maritime Column throughout a greater depth, they are not as high as a factor of 2 or more increases in extinction from HSRL-2. For the free troposphere aerosol layer in the Cape Cod column, there is a region of peak PM1 as high as 5 μg m^{-3} at the same altitude as the peak HSRL-2 extinction. The profiles of RH also suggest that aerosol water likely plays an important role contributing to observed extinction. The residual layer RH in the Maritime Column is usually between 70 and 95% while the RH in the Cape Cod Column is usually between 50 and 75% indicating the transport of drier continental air over the ocean. The higher humidity in the Maritime Column likely led to more water uptake that also increases extinction in addition to changes in the dry aerosol mass. In the Cape Cod Column, the median observed RH around 3.5 km is ~85%, while the median RH 1 km lower is much drier and closer to 50%. This also suggests that uptake of water by aerosols in the free troposphere layer could have contributed to the peak extinction at that altitude.

Table 3. Observed Biomass Burning (BB) Fraction and Volume Within the Cape Cod (CC) and Maritime (M) Columns Obtained From miniSPLAT As Well As Simulated Biomass Burning Quantities From WRF-Chem[a]

					Flight Day in July					
	Column	9	13	14	15	17	18	21	22	23	25
Observed BB	CC	7.69	4.69	7.15	11.93	8.70	9.36	6.27	5.10	5.07	3.03
Fraction (%)	M	6.98	8.25	7.43	7.51	7.35	8.37	4.59	4.62	5.30	4.39
Model BB	CC	1.05	0.47	0.49	0.97	9.20	7.08	14.92	18.59	7.14	49.70
Fraction (%)	M	2.20	0.64	0.81	2.16	2.35	3.13	12.18	11.27	10.63	55.25
Model BBOA	CC	0.11	0.05	0.06	0.10	1.04	0.82	1.76	3.53	0.08	5.56
Fraction (%)	M	0.20	0.05	0.08	0.26	0.28	0.37	1.27	1.70	1.39	8.68
Model BBSOA	CC	0.94	0.41	0.43	0.88	8.15	6.25	13.15	15.06	6.31	44.14
Fraction (%)	M	2.00	0.59	0.73	1.89	2.07	2.76	10.92	9.57	9.25	46.57
Observed BB	CC	0.074	0.231	0.293	0.383	0.235	0.366	0.082	0.118	0.241	0.037
Volume (μm^{-3}, cm^{-3})	M	0.185	0.225	0.375	0.347	0.260	0.352	0.075	0.131	0.164	0.066
Model BB	CC	0.012	0.052	0.062	0.087	0.409	0.613	0.220	1.151	0.948	2.688
Volume (μm^{-3}, cm^{-3})	M	0.095	0.037	0.065	0.156	0.329	0.627	0.199	0.435	0.873	7.108
Model BBOA	CC	0.001	0.006	0.007	0.009	0.054	0.071	0.026	0.234	0.109	0.301
Volume (μm^{-3}, cm^{-3})	M	0.009	0.004	0.007	0.019	0.044	0.084	0.021	0.071	0.111	1.210
Model BBSOA	CC	0.011	0.045	0.054	0.078	0.355	0.542	0.195	0.916	0.838	2.388
Volume (μm^{-3}, cm^{-3})	M	0.086	0.032	0.058	0.137	0.286	0.543	0.178	0.365	0.762	5.898

[a]BBOA and BBSOA denote primary and secondary biomass burning aerosols.

To understand the source of the errors in the simulated extinction profiles, Figure 10 also includes the simulated quantities from WRF-Chem and CAM5. Simulated PM1 (Figure 10a) from WRF-Chem is usually much higher than observed in the residual layer. Simulated concentrations in the Maritime Column are often twice as high as observed, while the near-surface concentrations in the Cape Cod Column are 3 times higher than observed. In contrast, PM1 from CAM5 is much closer to observed in the Maritime Column, except within 150 m of the surface where it is a factor of 2 too high. The profile of PM1 from CAM5 is also closer to observations than WRF-Chem in the Cape Cod Column residual layer, although CAM5's concentrations are 2 to 3 $\mu g\,m^{-3}$ too high. Both models produce PM1 concentrations in the Cape Cod Column above 1.8 km that are within the range of observed median values; however, neither model produces an appreciable peak on aerosol concentrations that are observed around 3.4 km, consistent with the errors in extinction at that altitude. Figures 10b–10f show that the overprediction in PM1 from WRF-Chem is not due to one aerosol component. OM, SO_4, NH_4, NO_3, and BC are all too high in the Maritime Column although NO_3 is a small portion of the total mass. Simulated biomass burning aerosol is relatively small and similar to measurements, as indicated in Table 3 and Figure S14, so that uncertainties associated with smoke are not a large factor contributing to the overprediction in OM. While PM1 from CAM5 is similar to observations in the Maritime Column, it does so for the wrong reasons: the low biases in OM and BC are compensated by overpredictions in SO_4 and NH_4. SO_4 and NH_4 also contribute to the positive PM1 bias in the Cape Cod Column residual layer where simulated OM and BC are closer to observed. Differences in the observed and simulated thermodynamic structure (Figure 10g) likely contribute to some of the discrepancies in the simulated aerosol profiles. The observed transition zone is characterized by smaller vertical gradients in θ; however, both models indicate a sharp transition between the residual layer and free troposphere so that the simulated θ is up to 2 K higher than observed, above 1.8 and 2.4 km in the Cape Cod and Maritime Columns, respectively. These temperature biases in the Maritime Column transition zone likely contribute to the underpredictions in RH from both models (Figure 10h). Simulated RH from both models in the Maritime Column residual layer is much closer to observations. The high humidity in this layer leads to simulated aerosol water (Figure 10i) with peak median values of 6 and 8 $\mu g\,m^{-3}$ from CAM5 and WRF-Chem, respectively. The lower RH in the Cape Cod Column results in little to no aerosol water in the Cape Cod Column. Little aerosol water is also produced in the Cape Cod free troposphere aerosol layer even though the observed RH is around 85%.

In addition to aerosol mass concentration and composition, aerosol size distribution is an important factor that affects the optical properties of aerosols. Figure 11 depicts the observed and simulated size distributed number and volume averaged over the entire G-1 flight as well as within the residual layer for the Cape Cod and Maritime Columns. Simulated aerosol volume is divided into the fraction resulting from each aerosol
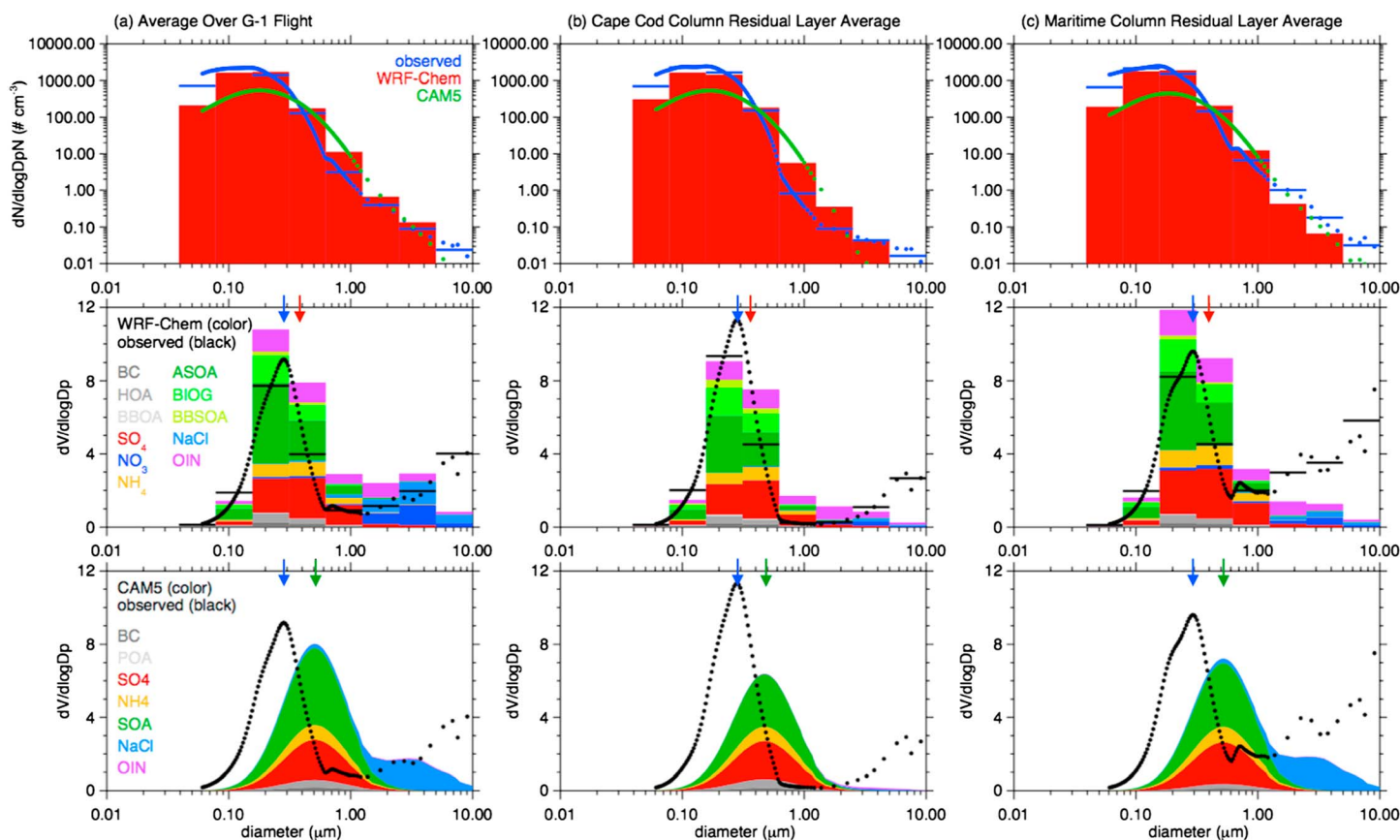
Figure 11. Observed and simulated size distribution of aerosol number and volume for the G-1 flight on 17 July averaged (a) over the entire G-1 flight, (b) within the Cape Cod residual layer, and (c) within the Maritime Column residual layer. Color shading for the simulated volume distributions denotes the fraction from each aerosol component. The arrows in the lower two rows denote the observed (blue). WRF-Chem (red), and CAM5 (green) mean diameters. The horizontal black lines in the middle panels denote observed averages within the size bins used by WRF-Chem.

species. In general, the number and volume distribution from WRF-Chem is closer to the observations than CAM5 (Figure 11a). In WRF-Chem, peak number concentrations occur in bins 2 and 3 (0.078–0.313 μm) and peak volume distributions occur in bins 3 and 4 (0.156–0.625 μm). Errors in the simulated size distribution from WRF-Chem vary in space and time as seem by comparing the Cape Cod (Figure 11b) and Maritime (Figure 11c) Columns. Simulated volume is too high for bins 4–6 (0.313–0.625 μm) in the Cape Cod column, while the simulated volume is too high for bins 3–5 (0.156–1.25 μm) and too low for bins 6–8 (1.25–10 μm) in the Maritime Column. Biases in the simulated residual layer PM1 in the Cape Cod Column offset each other (Figure 10a) so that the observed and simulated average total volume is similar; however, the simulated mean diameter of 0.374 μm is somewhat larger than the observed value of 0.282 μm. In the Maritime Column (Figure 11c), the simulated volume <1.25 μm is too high consistent with the PM1 profiles (Figure 10a), and as with the Cape Cod Column the mean diameter is larger than observed. The observed mean diameter increases by 0.009 μm from 0.282 to 0.290 μm between the Cape Cod and Maritime Columns, while the simulated mean diameter increases by 0.022 μm from 0.374 to 0.396 μm. The increase in diameter suggests that particles are growing (aging) as air parcels are transported from Cape Cod over the ocean, but the variations in diameter may also be due to different aerosol populations. The high aerosol volume for coarser particles occurs primarily for the flight legs closest to the ocean surface between 100 and 150 m, suggesting that WRF-Chem underestimates sea salt emissions and/or their turbulent mixing up to the aircraft altitude. Simulated sea salt adjacent to the ocean is often a factor of 2 higher than the values along the lowest flight tracks (not shown), suggesting that errors in the stability and turbulence within the shallow marine boundary layer are largely responsible for the underprediction of coarse aerosols. CAM5 also produces low concentrations of other inorganics, OIN, compared to WRF-Chem. As mentioned previously, WRF-Chem uses boundary conditions of dust from MOZART climatological values that may not be representative for this period.

For CAM5, the diameters of the peak number concentrations are similar to the observations; however, the aerosol number in the 80–320 nm range is much lower than observed so that the volume mean diameter is ~0.2 μm larger than observed. If the simulated submicron aerosol number were eight times higher, the number and volume curves would both shift toward the left and become closer to the observations. As with WRF-Chem, the lower than observed volume for coarse aerosols from CAM5 can be attributed to errors associated with sea salt emissions and vertical mixing.

We note that both models underestimate aerosol number concentrations for the smallest diameters, indicating that new particle formation is likely underestimated that subsequently affects the growth of particles to Aiken mode size. However, the observed and simulated mass less than 0.078 μm is very small and the simulated average volume in bin 2 (0.078–0.156 μm) is only 23% lower than observed. We note that errors in the simulated size distribution for small aerosols do not contribute significantly to extinction compared to larger aerosols with diameters closer to 1 μm.

3.3. Processes Contributing to Aerosol Layers on 17 July

Next we investigate the processes responsible for the free troposphere aerosol layer in the Cape Cod Column. Aerosol layers aloft, such as the one on 17 July, could result from long-range transport of aerosols from sources in Asia, regional-scale transport of aerosols from sources in North America, or from local transport of aerosols originating in the vicinity of the TCAP sampling domain. We use the FLEXPART model [*Brioude et al.*, 2013] for WRF-Chem and the Lagrangian Analysis Tool LAGRANTO version 2.0 for CAM5 [*Sprenger and Wernli*, 2015] to compute a 7 day back trajectory that starts at 17 UTC 17 July at an altitude of 4.5 km msl in the Cape Cod Column. The hourly locations of the back trajectories are based on the mean horizontal and vertical winds simulated by WRF-Chem. The back trajectory is shown in Figure 12a, along with the spatial distribution of PM2.5 and winds simulated by WRF-Chem at ~4.5 km msl. The altitude of the back trajectory and the vertical profiles of simulated PM2.5 along the back trajectory are shown in Figure 12b. As seen in Figure 12a, the aerosol layer produced by WRF-Chem (Figure 8b) is part of a region of PM2.5 concentrations exceeding 3 μg m^{-3} that extends over eastern Massachusetts, New Hampshire, Maine, and the Gulf of Maine. Cape Cod is on the edge of this plume. These results suggest that small transport errors may be responsible for the simulated extinction being too low over Cape Cod. The presence of lower PM2.5 concentrations ahead of this plume also indicates that the simulated plume arrived sooner than observed.

The back trajectory suggests that the aerosol layer was produced by rising motions starting at 17 UTC 16 July, which transported aerosols from the boundary layer up to an altitude of 5 km in 6 h. The stronger westerly and northwesterly winds at this altitude quickly transported the aerosol layer over Cape Cod in about 18 h. Therefore, a large fraction of the aerosols are likely about a day old, although the descending air along the back trajectory between 11 and 16 July indicates that long transport of small concentrations ($<$1 μg m^{-3}) of aged aerosols were mixed with the fresher boundary layer aerosols prior to their lifting back into the midtroposphere. As shown in Figure 12b, clouds were simulated in the vicinity of the lifting of aerosols and in the path of the aerosol layer. Therefore, wet scavenging may have reduced the concentration of aerosols before the layer passed over Cape Cod. Figure 12a also shows small regions of PM2.5 exceeding 4 mg m^{-3} over Missouri and the southeastern U.S. These regions result from vertical transport within deep convective clouds parameterized by KF-CuP, demonstrating that convection quickly transports boundary layer aerosols into the middle to upper troposphere.

A back trajectory from CAM5 that starts at the same time and location is similar to WRF-Chem for about 1.5 days. Figure 12c shows that lifting also occurs at the same time and general location around Lake Superior as in WRF-Chem, except that the vertical velocities are lower so that lifting occurs over a longer period. While aerosol concentrations greater than 6 μg m^{-3} are produced 3 to 5 km above the ground, wet scavenging processes in clouds remove most of these aerosols so that only low concentrations arrive at Cape Cod several hours later.

We now illustrate the processes responsible for lifting aerosols into the free troposphere in Figure 13. This figure shows the simulated PM2.5 and vertical velocities at ~3.4 km msl over the Great Lakes at 18 UTC 16 July (Figure 13a) along with vertical cross sections of PM2.5 and vertical velocities (Figure 13b), horizontal wind components (Figure 13c), and θ and cloud-borne aerosol concentrations (Figure 13d) averaged between 45° and 48°N. At this time, PM2.5 concentrations exceeding 3 μg m^{-3} are produced over central Lake
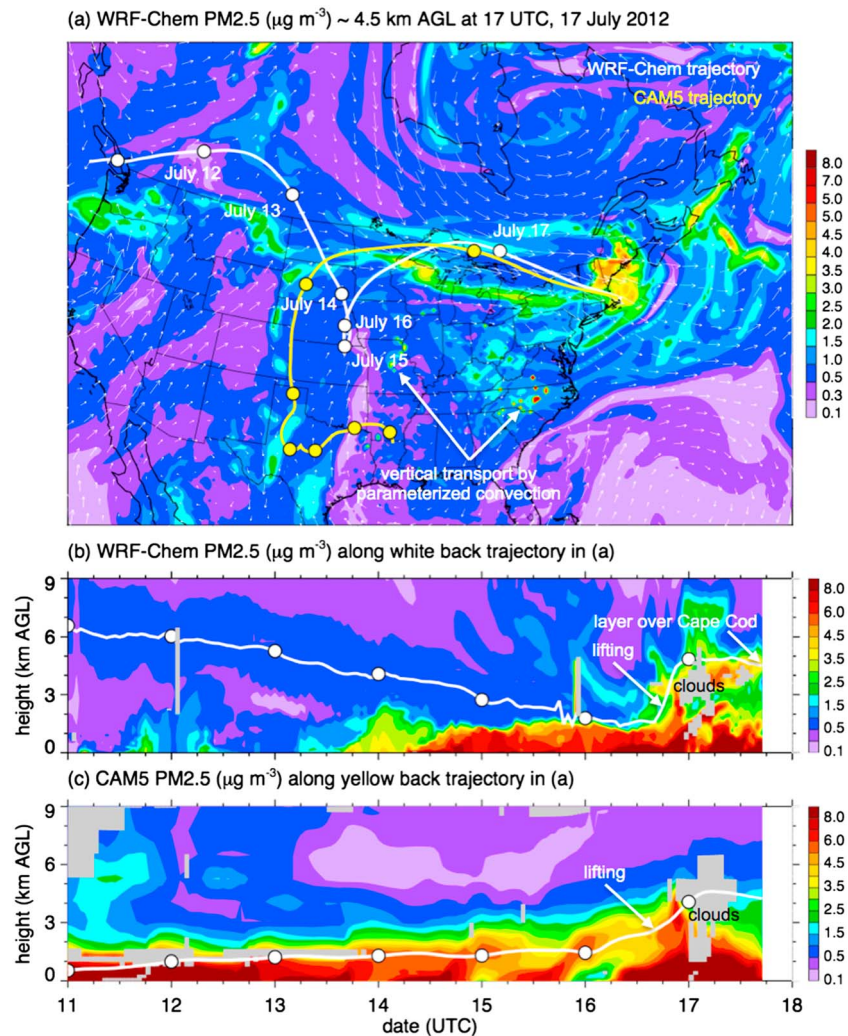
Figure 12. (a) PM2.5 simulated by WRF-Chem over the outer nested domain at ~4.5 km msl at 17 UTC 17 July along with a back trajectory from WRF-Chem (white line) and CAM5 (yellow line) originating over the Cape Cod at this time. Simulated PM2.5 profiles along the (b) WRF-Chem and (c) CAM5 trajectories are shown, back between 11 and 17 July 11 along with the altitude of the back trajectory. Gray shading in Figure 12b denotes grid cells with simulated resolved and parameterized clouds and in Figure 12c denotes cloud fraction > 25%.

Superior and parts of southwestern Ontario (Figure 13a). The highest PM concentrations coincide with vertical velocities greater than $10 \, cm \, s^{-1}$ and in some regions vertical velocities are as high as $40 \, cm \, s^{-1}$. The vertical cross section of PM2.5 (Figure 13b) also shows the aerosol layer forming at the same altitudes as the highest upward mean vertical velocities. Simulated aerosol concentrations greater than $1 \, \mu g \, m^{-3}$ are lifted up to 9 km msl between $-86°$ and $-81°W$. While velocities on the order of tens of $cm \, s^{-1}$ may seem small, an air parcel can be lifted over 2 km over 6 h by $10 \, cm \, s^{-1}$ rising vertical motions. As the aerosol layer is lifted, it encounters stronger westerly winds as high as $25 \, m \, s^{-1}$ at an altitude of 4 to 5 km msl. These results suggest that one reason for the free troposphere aerosol layer arriving at too high of an altitude and too early over Cape Cod is that the mean vertical velocities in this convergence zone are too large. If the simulated upward vertical velocities are too large, aerosols would be lifted to a higher altitude than in reality. Had the aerosols been transported to a lower altitude, the westerly winds would also be weaker so that the aerosol layer would arrive later and closer to observed arrival over Cape Cod. Figure 13d shows that WRF-Chem predicts grid-resolved clouds (from the microphysics parameterization) to form at the same altitudes as the higher PM2.5 concentrations in the aerosol layer. These clouds are not precipitating at this time, but some of the resolved clouds north of Lake Superior are precipitating (not shown) and would act to remove some of the
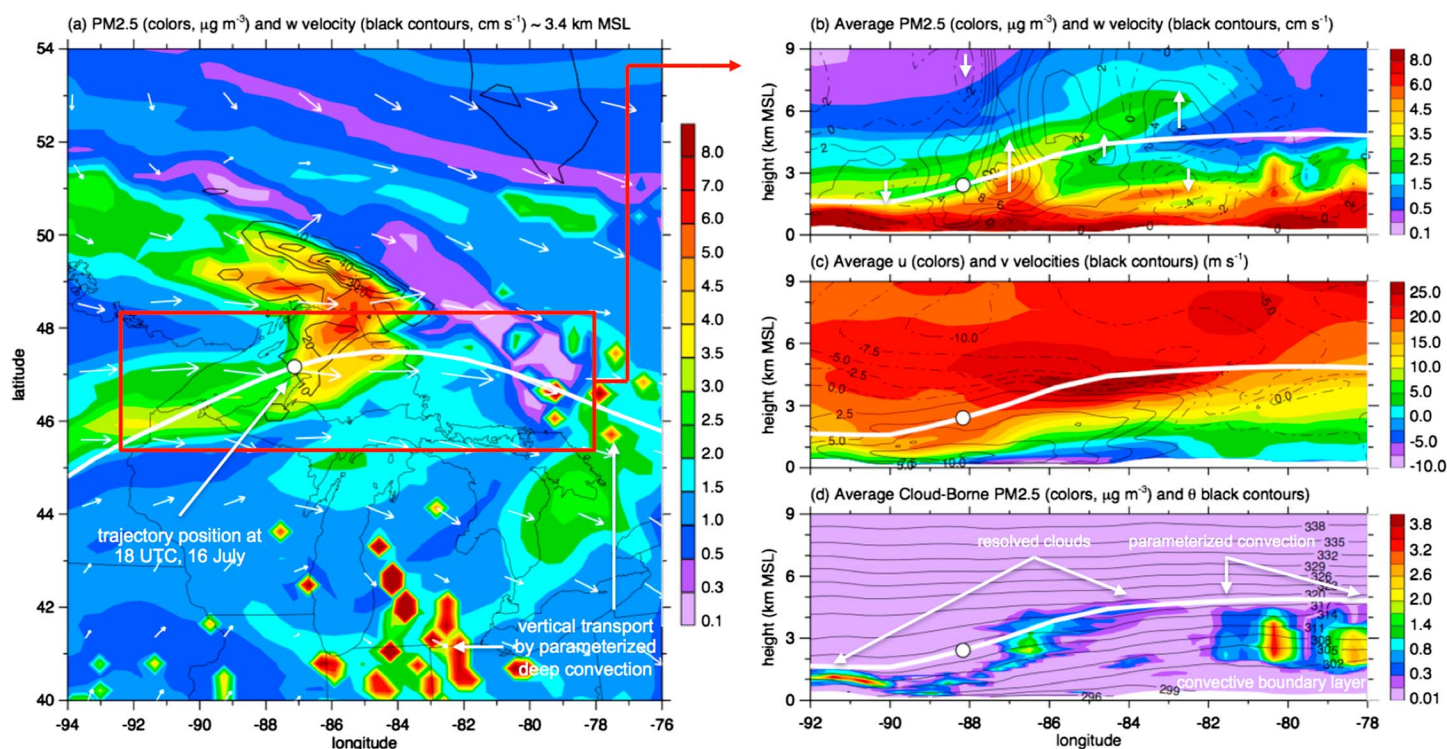
Figure 13. (a) PM2.5 (color) and upward vertical velocities (black contours) simulated by WRF-Chem over the Great Lakes region at ~3.4 km msl at 18 UTC 16 July along with vertical cross sections of (b) PM2.5 (color) and vertical velocities (black lines), (c) u (color) and v (black lines) wind components, and (d) cloud-borne aerosol concentrations (color) and q (black lines) that are north-south averages within the red box in Figure 13a. The white line depicts the back trajectory shown in Figure 11.

PM2.5 in this region. At this time, parameterized deep convection occurs east of 82°W, which transports boundary layer aerosols up to 4.5 km msl, but they do not intersect the midtropospheric aerosol layer at this time.

CAM5 also produced a region of upward vertical motions in the vicinity of Lake Superior where WRF-Chem predicted 5 to 40 cm s^{-1} (Figure 13a); however, the velocities from CAM5 were only as high as 5 to 10 cm s^{-1} (not shown). Not surprisingly, coarser spatial resolution results in less convergence and hence smaller upward vertical motions so that near-surface aerosols are not lifted as fast as regional models, such as WRF-Chem. This result is also consistent with more of the aerosol mass being located in the lower troposphere compared to observations (Figures 4 and 6).

In addition to the back trajectory, the peak NO$_3$ concentrations in the Cape Cod free troposphere layer (Figure 10d) also hints at a source in the upper Midwest. The band of higher PM2.5 that extends from central Minnesota to northern Wisconsin and Lake Superior (Figure 13a) contains NO$_3$ concentrations as high as 3 μg m^{-3}. Emissions of ammonia likely contribute to NO$_3$ formation in this rural region. As the aerosol layer is transported up to 3 to 5 km, NO$_3$ does not quickly partition back into the gas phase due to the colder temperatures. The wind fields in Figure 13a show that the band of PM2.5 simulated just north of Minnesota is being transported toward Lake Superior. This band of PM2.5 contains concentrations of biomass burning aerosol that are 1 μg m^{-3} or less at this altitude. While these concentrations are low, this band is actually the top of a larger biomass burning plume with higher concentrations located farther to the north and at lower altitudes. Thus, smoke from Canadian fires converge and mix with NO$_3$-rich air over Lake Superior and contribute to the biomass burning aerosols observed in the Cape Cod free troposphere layer (Figure S14).

Back trajectories in the residual layer of the Maritime and Cape Cod Columns are more complex, showing clockwise recirculation around a high-pressure system over the northeastern U.S. prior to air masses arriving in the TCAP sampling domain [see *Berg et al.*, 2016, Figure 11b]. Differences in the trajectories in the Cape Cod and Maritime Columns also indicate different source regions likely contributed to the aerosol burden in each
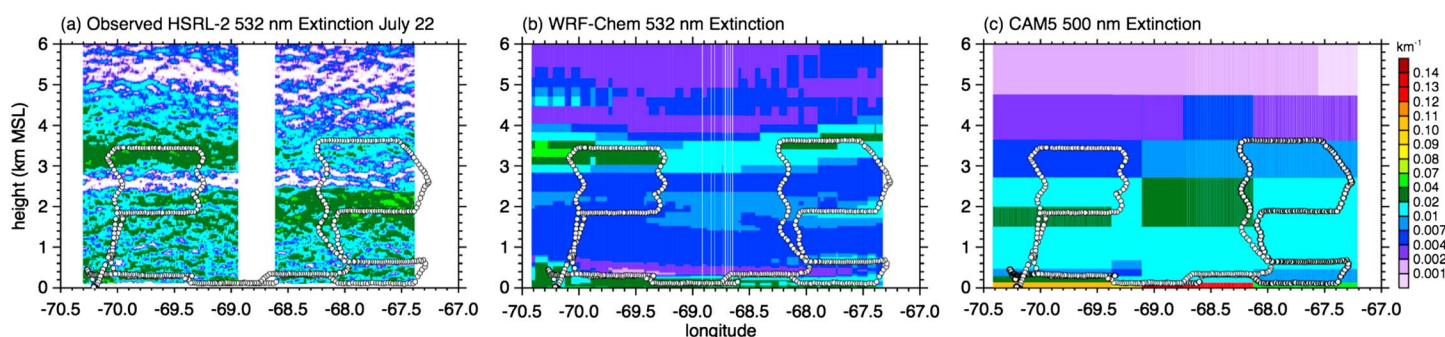
Figure 14. Extinction profiles on 22 July as a function of longitude between 1527 and 1615 UTC (a) observed by HSRL-2 and simulated by (b) WRF-Chem and (c) CAM5. The dots denote the sampling altitude of the G-1 aircraft during the entire flight.

column. The longer residence time (more than 7 days) of the trajectories in the boundary layer over the anthropogenic emission sources also suggests that aerosols in the residual layer are more aged than the free troposphere layer (Figure 8a).

3.4. Layering During the 22 July Clean Period

We next examine observed and simulated aerosol layering on 22 July when the aerosol concentrations were much lower as a result of the synoptic conditions being less conducive for transport from high emission sources along the East Coast urban corridor. On this day, the ambient winds over the AMF site were southerly to southwesterly below 2 km, northwesterly from 2 to 4 km, and westerly above 5 km and northwesterly above that altitude (Figure S1); therefore, the aircraft flight paths were across the wind direction at most altitudes (Figure 1). Four layers of aerosols were observed by the HSRL-2 on this day and two of them between 1527 and 1615 UTC are shown in Figure 14a. The first is a layer that encompasses the entire west-east cross section between 1.4 and 2.4 km with the highest extinction in the Maritime Column and corresponds to the southwesterly winds that transition to westerly winds at the top of that aerosol layer. The second layer associated with the northwesterly winds occurs in the Cape Cod column between 2.6 and 5 km, with the highest extinction around 3.2 km. This layer extends to the east into the Maritime Column but decreases in magnitude and depth. A third layer in the backscatter profiles, shown in Figure 6b in *Berg et al.* [2016], occurs within a 0.2 to 0.3 km of the ocean surface over the entire transect. A fourth, thin layer at 0.8 km in the backscatter profiles is as much as 0.2 km thick and extends from the western boundary to −68.5°W. The thinner third and fourth layers can be seen in the backscatter profiles but not the extinction profiles, because extinction requires a somewhat longer sampling time that smooths out these thin layers. Although the magnitude of the extinction changed somewhat during the 3.5 h flight period, the structure of these layers did not change very much in contrast to 17 July. Most notably, extinction diminished in the Maritime Column layer between 3 and 4 km and the extinction increased somewhat at the same altitude in the Cape Cod Column by the end of the sampling period. We note that missing data between −69.0 and −68.5 W is due to aircraft turns in which the lidar is blocked for eye safety reasons.

Figures 14b and 14c show the simulated extinction profiles for the same time from WRF-Chem and CAM5, respectively. While both models qualitatively represent the layering there are notable differences between the models and the HSRL-2 observations. The uppermost layer simulated by WRF-Chem (Figure 14b) is located at the correct altitude, and the extinction magnitude is similar to the measurement, although the depth in the Cape Cod Column is somewhat shallower than observed. Extinction in the layer below 2.4 km is too low by a factor of 2 to 3. Strong gradients in aerosol concentrations are produced over the Gulf of Maine with higher concentrations just northwest of the G-1 flight path and lower concentrations along and southeast of the flight path. Therefore, the underprediction in the extinction is due to small errors in the simulated horizontal transport. WRF-Chem is able to produce a shallow aerosol layer adjacent to the ocean surface that is similar to observations and a thin layer at 0.8 km that was also observed. In contrast, the extinction from CAM5 in the layer below 2.8 km is closer to observed than WRF-Chem, although extinction in a shallow layer adjacent to the ocean surface is much higher than observed. Note that differences in the observed residual layer boundary at 2.4 km and CAM's boundary at 2.8 km are likely due to the coarser
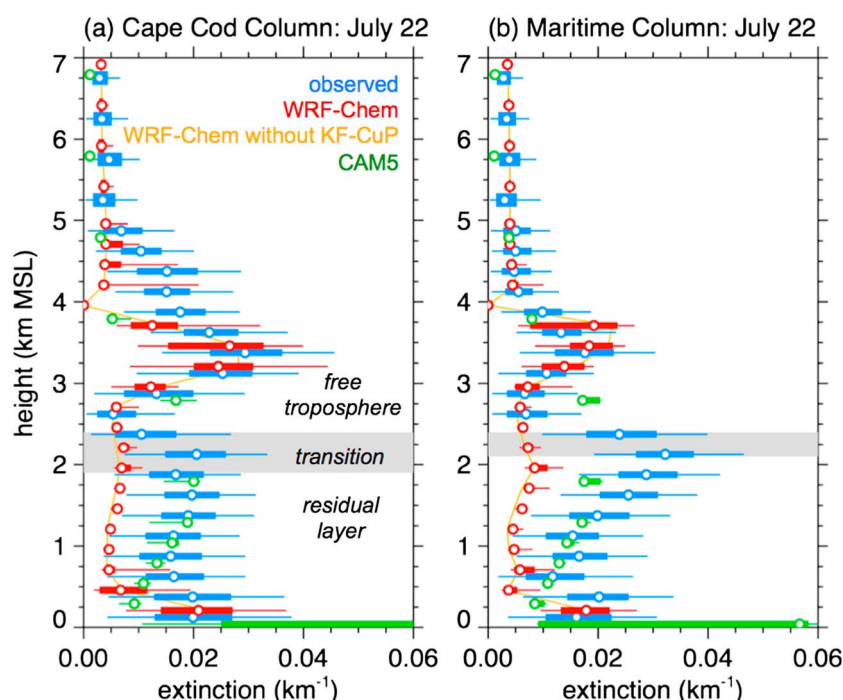
Figure 15. Vertical profiles of observed (blue) and simulated extinction from WRF-Chem (red) and CAM5 (green) in the (a) Cape Cod Column and (b) Maritime Column on 22 July. The dots are the median, the horizontal bars are the 25th to 75th percentiles, and the horizontal lines are the 5th to 95th percentiles. The orange line is from the WRF-Chem simulation without the effect of KF-CuP on aerosols.

vertical grid spacing in CAM5. Extinction in CAM5 gradually decreases to low values in the free troposphere that does not resemble the observed layer between 2.8 and 5 km.

A quantitative assessment of the simulated extinction profiles over the entire 22 July flight period is shown for the Cape Cod and Maritime Columns is Figures 15a and 15b, respectively. Similar to 17 July, the transition zone between the residual layer and the free troposphere denoted by gray shading is based on both changes in the vertical potential temperature, θ, and relative humidity (RH) gradients from the aircraft observations (Figures 16g and 16h). For WRF-Chem the median and range of values for the free troposphere aerosol layer in both columns are close to the measurements at the altitude of the peak extinction; however, the depth of the layer is shallower than observed in the Cape Cod Column. While the simulated extinction is close to observed near the ocean surface, the extinction throughout much of the residual layer is a factor of 2 to 3.5 too low in both columns due to a small error in the placement of the band of aerosols over the Gulf of Maine. CAM5 has median values that are closer to the observations than WRF-Chem, but the extinction at the ocean surface is much higher than observed and it does not produce the observed aerosol layer in the free troposphere.

The associated in situ G-1 measurements for this flight are shown in Figure 16. WRF-Chem does produce a peak value of PM1 in the free troposphere that occurs at the same altitude as observed in both the Cape Cod and Maritime Columns (Figure 16a); however, the concentrations are somewhat higher than observed. It is possible that the high bias in dry mass is offset by the low bias in RH (Figure 16h) that would lead to aerosol water being too low. Consistent with extinction, simulated PM1 in the residual layer is lower than observed by similar magnitudes as extinction except close to the ocean surface. The residual layer dry PM1 mass from CAM5 is closer to observed than WRF-Chem, consistent with the extinction profiles. While simulated OM is responsible for much of the low bias in the residual layer PM1 in WRF-Chem, the profile of simulated OM from CAM5 is similar to the observations (Figure 16b). In contrast, SO_4 from both models is higher than observed by a factor of 2 to 3, (Figure 16c). While WRF-Chem fails to produce NO_3 in the residual layer, peak values of NO_3 are produced in the free troposphere layer although the simulated concentrations are too high (Figure 16d). In contrast, simulated NH_4 and BC (Figures 16e and 16f) from WRF-Chem are closer to
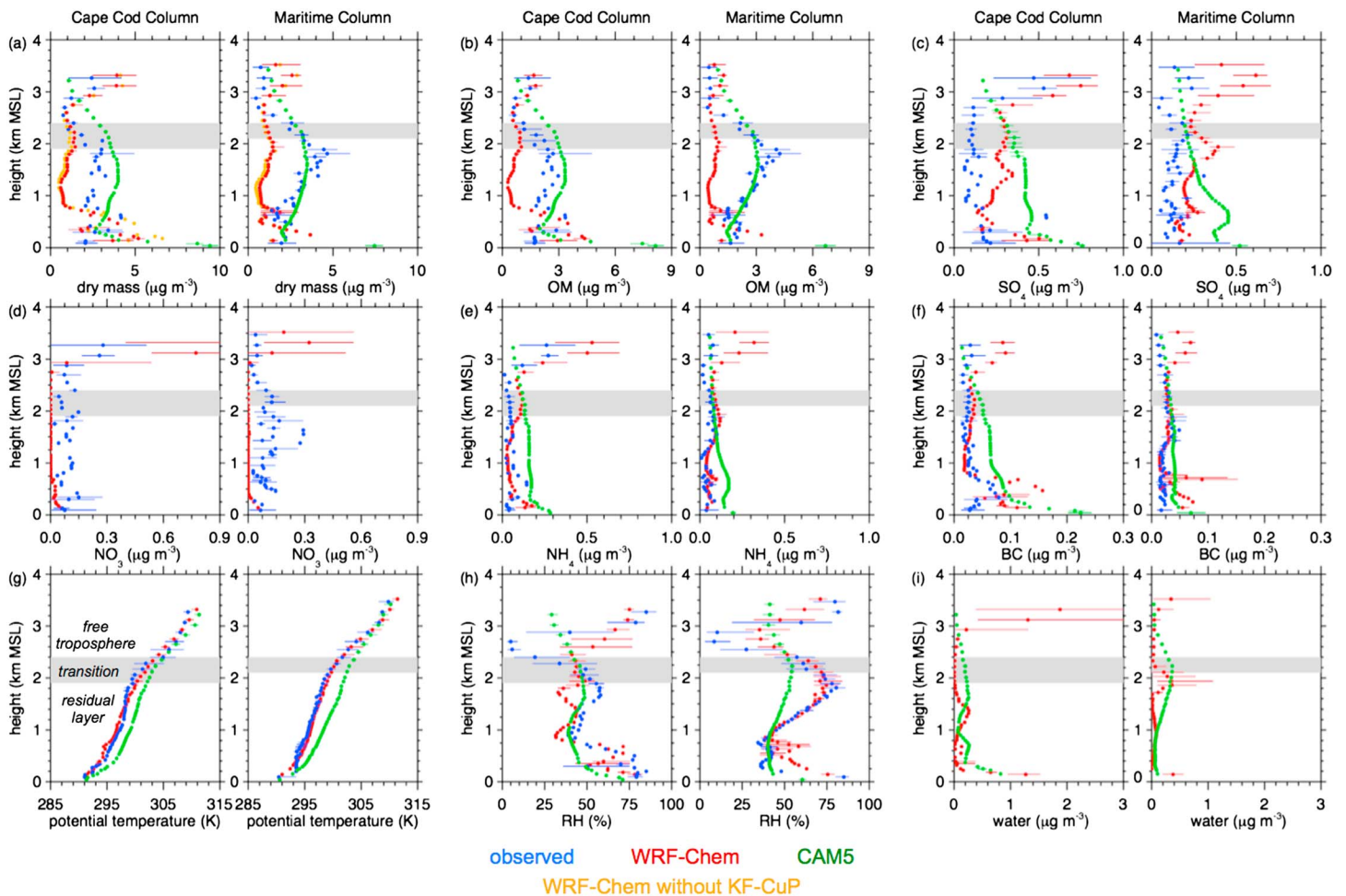
Figure 16. Observed and simulated profiles of (a) PM1 mass, (b) organic matter, (c) sulfate, (d) nitrate, (e) ammonium, (f) black carbon, (g) potential temperature, θ, (h) relative humidity, RH, and (i) aerosol water for the G-1 flight on 22 July. Dots and horizontal lines denote the average and range, respectively, at each altitude. Only PM1 is shown for the WRF-Chem simulation without KF-CuP. Nitrate is not simulated by CAM5.

observed profiles than other aerosol species, except in the free troposphere where the concentrations are also too high, and simulated NH_4 and BC from CAM5 is usually higher than observed. The WRF-Chem simulated profiles of θ are very similar to the aircraft measurements (Figure 16g), but profiles from CAM5 are usually 1 to 3° higher than observed in the residual layer. These errors do not likely contribute to errors in the aerosol layers because the overall structure in the residual and free troposphere drives the structure of the aerosol layers, of more importance is that errors in temperature contribute to the low bias in residual layer RH (Figure 16h) that will affect the uptake of water on aerosols (Figure 16i).

The observed and simulated size distributions for number and volume averaged over the entire G-1 flight as well as within the residual layer for the Cape Cod and Maritime Columns are shown in Figure 17. The performance of WRF-Chem and CAM5 in representing the observed size distribution is similar in many respects to their performance on 17 July. While WRF-Chem better represents the size distribution with the mean diameters closer to observations than CAM5, the aerosol number and volume are too low consistent with the aerosol concentrations and extinction shown previously. While the residual layer aerosol volume is closer to observed, the mean diameters are 0.2 to 0.3 μm higher than observed. Both models fail to produce higher aerosol volumes for diameters greater than 5 μm that are likely sea salt.

3.5. Processes Contributing to Aerosol Layers on 22 July

We next examine the processes contributing to the free troposphere aerosol layer observed in the Cape Cod Column. The back trajectory associated with this layer is shown in Figure 18a along with the spatial
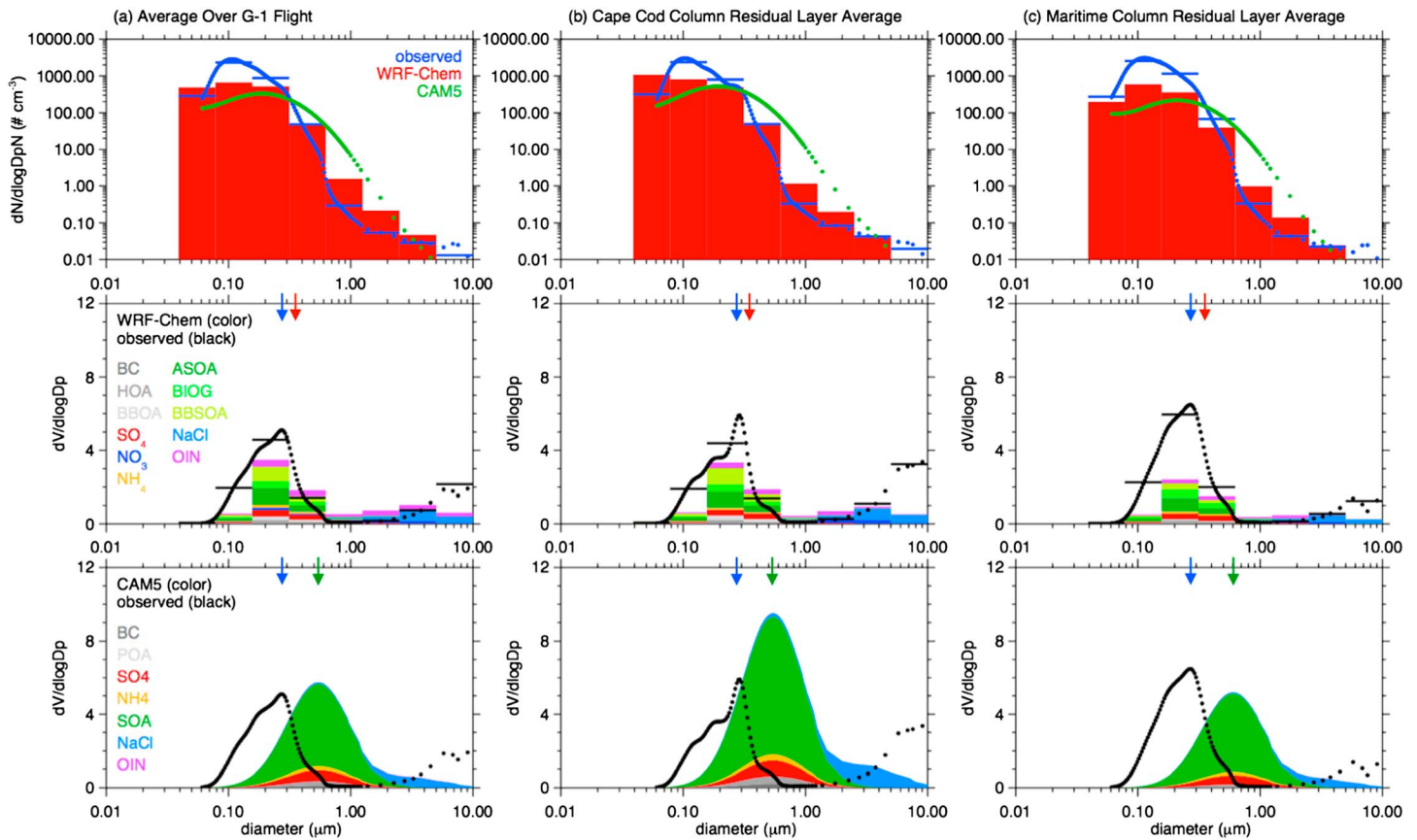
Figure 17. Observed and simulated size distribution of aerosol number and volume for the G-1 flight on 22 July averaged (a) over the entire G-1 flight, (b) within the Cape Cod residual layer, and (c) within the Maritime Column residual layer. Color shading for the simulated volume distributions denotes the fraction from each aerosol component. The arrows in the lower two rows denote the observed (blue), WRF-Chem (red), and CAM5 (green) mean diameters. The horizontal black lines in the middle panels denote observed averages within the size bins used by WRF-Chem.

distribution of PM2.5 and winds simulated by WRF-Chem at ~3.2 km msl, while Figure 18b shows the altitude of the back trajectory and the vertical profiles of simulated PM2.5 along the trajectory. The model suggests that the free tropospheric aerosols sampled at this time are part of a layer extending from New Jersey to southern Nova Scotia (Figure 18a). Bands of high aerosol concentrations $>8\,\mu g\,m^{-3}$ over Quebec and Hudson Bay produced by fires in western Canada, are circulated around a low-pressure system at this time but do not directly impact the TCAP sampling region.

The back trajectory suggests that the aerosol layer was produced by rising motions starting at 12 UTC 20 July, which transported aerosols from the boundary layer over northern Minnesota up to an altitude of 4 km over southern Ontario in 1 day (Figure 18b). The trajectory gradually descended over the next 27 h from 4 to 3 km as it was transported to the southeast by the synoptic-scale wind field, passing over Cape Cod at 17 UTC 22 July. Prior to the lifting of this layer, the trajectory suggests that air in the boundary layer was circulated over the northern Great Plains by light winds between 16 and 19 July. Low-pressure systems forming along a cold front extending from Canada into the northern Great Plains resulted in southerly winds transporting aerosols from Nebraska to North Dakota by 20 July. As the cold front pushed eastward on 20 July and into northwestern Minnesota on 21 July, near-surface winds became westerly and the air parcel started to rise as a result of lifting ahead of the front. In contrast with the 17 July case, CAM5 produces little to no lifting associated with this frontal system as shown in Figure 18c.

Figure 19 illustrates the lifting ahead of the cold front in more detail. Simulated PM2.5 and vertical velocities from WRF-Chem at 2 km msl are shown in Figure 19a, along with vertical cross sections of PM2.5 and vertical velocities (Figure 19b), horizontal wind components (Figure 19c), and potential temperature and cloud-borne aerosol concentrations (Figure 19d) averaged between 45° and 48°N. The lifting processes are similar to those
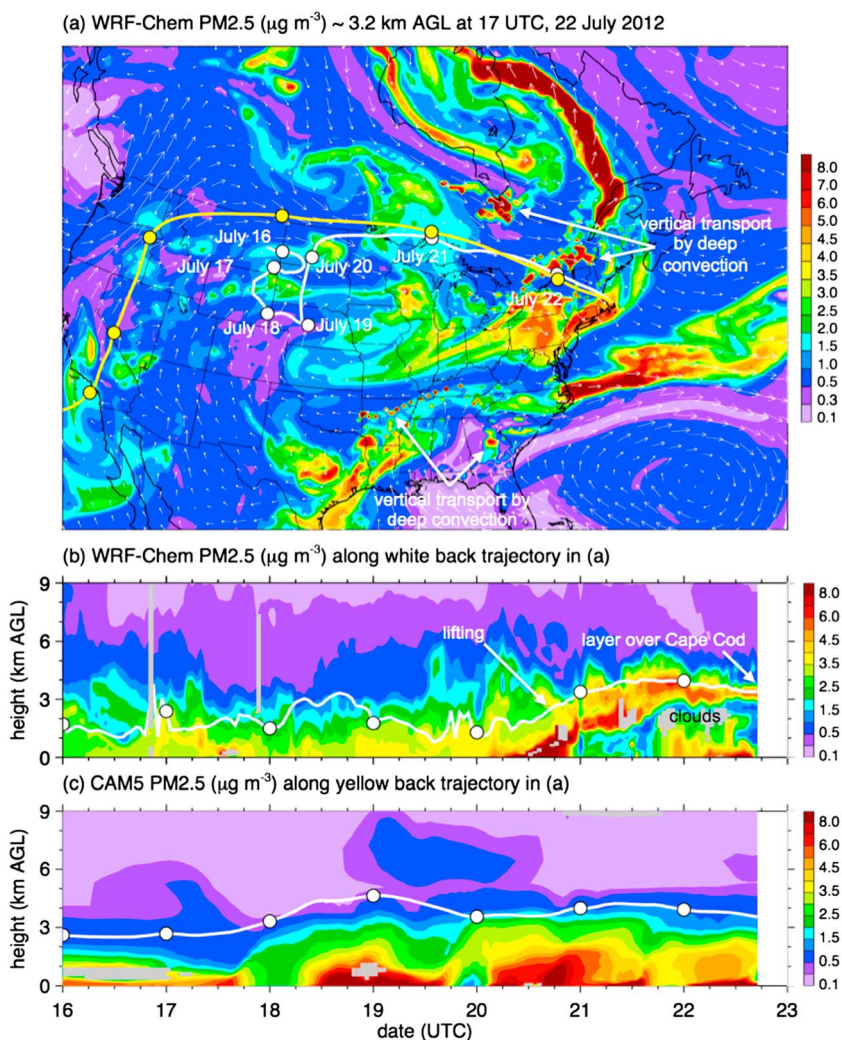
Figure 18. (a) PM2.5 simulated by WRF-Chem over the outer nested domain at ~3.2 km msl at 17 UTC 22 July along with a back trajectory from WRF-Chem (white line) and CAM5 (yellow line) originating over the Cape Cod at this time. Simulated PM2.5 profiles along the WRF-Chem and CAM5 trajectories are shown in Figures 18b and18c, respectively, back between 16 and 22 July along with the altitude of the back trajectory. Gray shading in Figure 18b denotes grid cells with simulated resolved and parameterized clouds and in Figure 18c denotes cloud fraction >25%.

discussed for the 17 July case, except that the vertical velocities associated with the higher PM2.5 concentrations are a few cm s^{-1} and there are only a few small regions in which they are greater than 10 cm s^{-1} in contrast with those on 16 July (Figure 13a), which are 10 cm s^{-1} or more over a large region. CAM5 also produces a band of upward vertical motions in this region, but they are usually weaker than those from WRF-Chem, with peak values of about 2 cm s^{-1} (not shown). The weaker rising motions lead to gradual ascent of aerosols over a longer period of time (Figure 19b). The wind speeds aloft (Figure 19c) are also much weaker than the other case that would transport this layer to Cape Cod over a longer period of time. Figure 19d shows that the trajectory passes over clouds forming closer to the surface. Some of these clouds are precipitating at this time that would remove aerosols, thus increasing the vertical gradient on PM2.5 with higher values aloft. Clouds north of the trajectory are also precipitating, indicating lifting ahead of the cold front, and near-surface wet removal would create a layer of aerosols aloft over a region stretching from South Dakota into Minnesota and western Ontario.

Similar to 17 July, the lifting and mixing processes in this region contribute to the peak NO$_3$ concentrations and presence of biomass burning aerosols observed in the free troposphere Cape Cod Column on 22 July (Figure 16d). The band of higher PM2.5 that extends from North and South Dakota, Minnesota, and southern
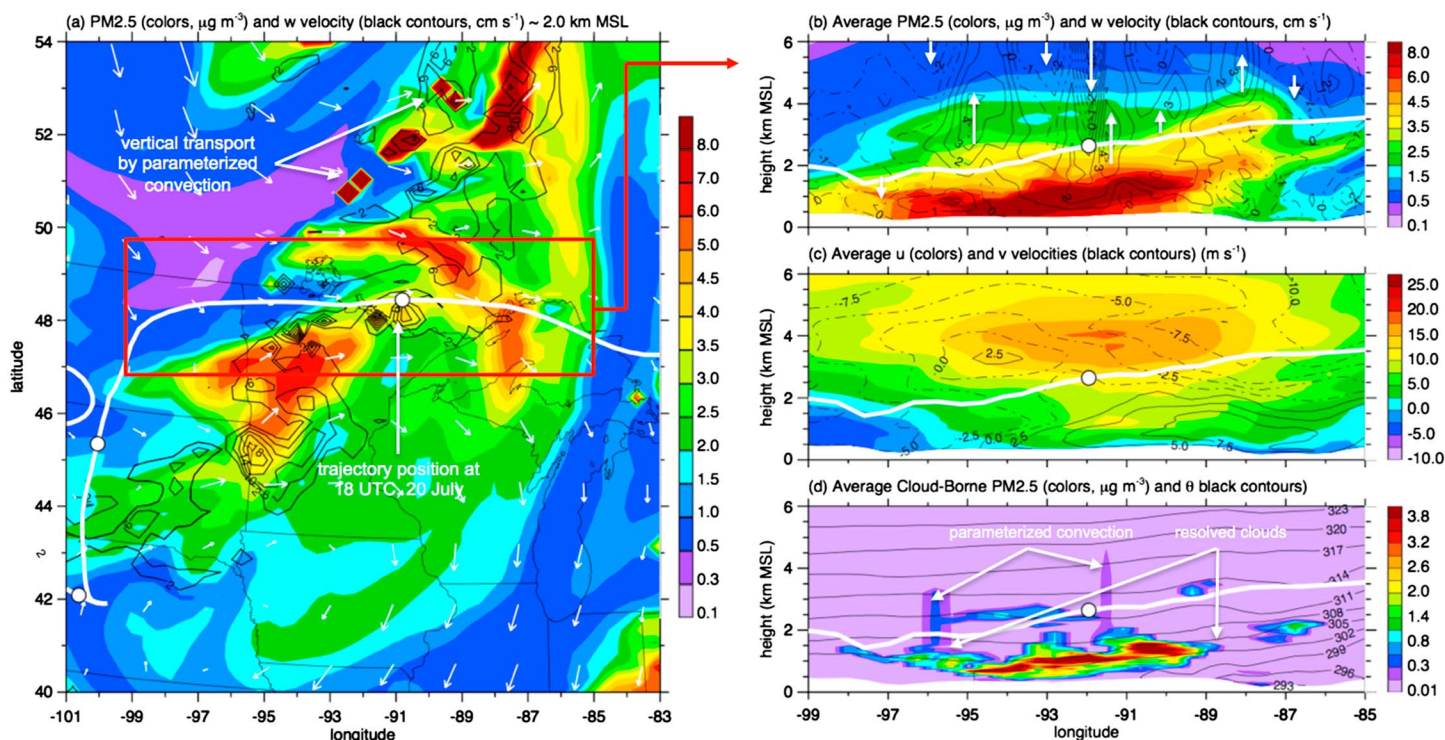
Figure 19. (a) PM2.5 (color) and upward vertical velocities (black contours) simulated by WRF-Chem over the north central at ~2.0 km msl at 18 UTC 20 July along with vertical cross sections of (b) PM2.5 (color) and vertical velocities (black lines), (c) u (color) and v (black lines) wind components, and (d) cloud-borne aerosol concentrations (color) and q (black lines) that are north-south averages within the red box in a). The white line depicts the back trajectory shown in Figure 17.

Canada (Figure 19a) in the vicinity of the back trajectory contains NO_3 concentrations as high as $1.8\,\mu g\,m^{-3}$. Biomass burning aerosol concentrations as high as $1.4\,\mu g\,m^{-3}$ are present in the PM2.5 plume over northwestern Minnesota, but not in the PM2.5 plume just north of Minnesota and over Lake Superior. While biomass burning fractions on 17 July were as high as 20% in the Cape Column, they are less than 10% above 3 km on 22 July (Figure S15). The simulated biomass burning is consistent with the miniSPLAT measurements on this day at this altitude. The model also suggests that the reason biomass burning fractions are lower on 22 July is that the highest concentrations of smoke do not intersect the central transport pathway on 20 July. The highest simulated PM2.5 concentrations north of Lake Superior contains biomass burning aerosols as high as $22\,\mu g\,m^{-3}$, but this band does not pass over the TCAP sampling domain.

3.6. Effects of Parameterized Convection on Aerosol Vertical Profiles and Layering

As we have shown in the previous section, mean vertical motions associated with synoptic-scale weather systems upwind of the TCAP sampling domain are responsible for lifting aerosols from the boundary layer into the free troposphere. These layers become decoupled from the boundary layer and are therefore not subject to fresh emissions of primary aerosol or aerosol precursors except for intense fires that lift smoke to high altitudes and aircraft emissions (not included in this study). The higher wind speeds at these altitudes permit the aerosol layers to be transported long distances unless they are removed by wet scavenging. Vertical transport by convection is another process that affects the redistribution of trace gases and aerosols in the atmosphere [e.g., *Barth et al.*, 2015]. We examined the impact of the KF-CuP parameterization on aerosol concentrations by performing a WRF-Chem sensitivity study that is identical to the previous model configuration except that the effect of parameterized clouds on trace gases and aerosols are turned off. KF-CuP is still activated to affect meteorological quantities, such as altering the thermodynamic profiles, producing rain, and reducing downward solar radiation reaching the surface.

The effect of parameterized convection influences the aerosol profiles differently on different days during TCAP. On 17 July, PM1 concentrations without KF-CuP are up to $3\,\mu g\,m^{-3}$ higher than the default simulation
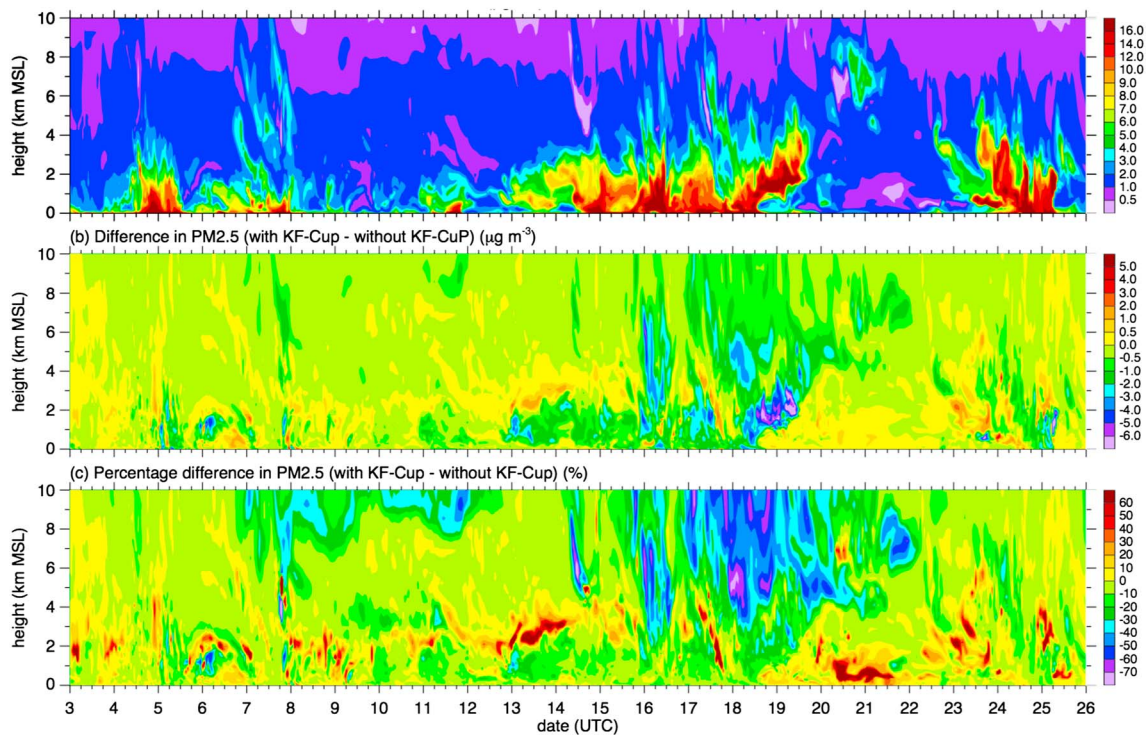
Figure 20. (a) Simulated PM2.5 over the Cape Cod site from the WRF-Chem simulation with KF-CuP affecting aerosols and gases, (b) absolute concentration differences for (KF-CuP affecting aerosols case)—(KF-CuP not affecting aerosols case), and (c) same as Figure 20b but expressed in terms of percentage differences.

in the Maritime Column as shown by the orange line in Figure 10a. In contrast, there is very little difference in the Cape Cod Column except that the simulation without KF-CuP produces somewhat lower PM1 between 1 and 2 km. The differences in PM1 are reflected in the changes in extinction as shown in Figure 9. While the aerosol concentration and extinction are different in the Maritime Column on this day, the parameterized convection does not affect the overlay layering of aerosols over the TCAP sampling domain. For 22 July, the effect of parameterized convection on aerosols has very little effect on the PM1 concentration (Figure 16a) and extinction profiles (Figure 15).

To examine the impact of KF-CuP on aerosols over the entire study period, Figure 20 shows the difference in simulated PM2.5 between the two simulations over the AMF site. Figure 20a shows the same vertical profiles of PM2.5 as in Figure 4a as a reference since the differences are proportional to the aerosol concentrations. The PM2.5 profiles from the simulation without the effect of KF-CuP on aerosols are qualitatively similar to Figure 20a, so they are not shown. The largest differences in PM2.5 are produced between 13 and 20 July (Figure 20b), which are associated with lower PM2.5 concentrations during a dirty period. In the default simulation, PM2.5 is 3 to $9 \, \mu g \, m^{-3}$ lower than the simulation without KF-CuP in regions from a few hundred meters above the surface to 7 km msl. Decreases in PM2.5 are also produced during the other dirty periods, but the decreases are usually confined to altitudes below 2 km. There are also regions in which the default simulation has higher PM2.5 concentrations. The regions with the largest increase in PM2.5 usually occur at 1–3 km in the lower troposphere, just above the typical height of the daytime continental boundary layer. When one examines the difference between the simulations in terms of percentage change, the differences become more apparent (Figure 20c). There are large percentage decreases in the middle to upper troposphere in which PM2.5 is lower by 30% or more in the default simulation. The PM2.5 concentrations in the middle to upper troposphere are relatively low and usually $2 \, \mu g \, m^{-3}$ or less, but the percentage change is often large. There are also regions in the lower troposphere in which the PM2.5 concentrations are relatively low but increase by 40% or more in the default simulation.

As described in *Berg et al.* [2015], vertical transport in the parameterized shallow convection of KF-CuP will have a net effect of moving aerosols out of the boundary layer to the detrainment level of the shallow clouds (near cloud top), assuming that aerosol concentrations are lower in the free troposphere. Shallow clouds are

assumed to not precipitate, so there is no wet removal of aerosols, but aqueous chemistry does occur that transforms the overall aerosol size and composition within those clouds. For parameterized deep convection, vertical transport occurs over a much deeper layer. Aerosols in updrafts experience strong wet removal, and the boundary layer aerosols transported by updrafts are efficiently removed, so aerosol concentrations in updrafts at the detrainment level (near cloud top) can be quite low. Below the updraft detrainment level, compensating subsidence transports generally cleaner air from the upper troposphere downward. With that in mind, the decreases in PM2.5 concentrations at 1–3 km in the lower troposphere are likely the result of parameterized shallow convection upwind of the TCAP sampling domain. The shallow convection would transport boundary layer aerosols into the lower troposphere in the default simulation, so that the PM2.5 concentrations just above cloud level are lower in the simulation without KF-CuP. Since shallow convection is occurring at various distances upwind of Cape Cod, its impact on PM2.5 would be altered by transport and mixing processes as well as chemical transformation so that the differences between the two simulations vary in time. The higher PM2.5 concentrations in the free troposphere from the simulation without KF-CuP occur because of the wet removal and subsidence. The relative change in free troposphere PM2.5 concentrations depend on whether the air parcels pass through upwind cells in which parameterized convection is activated. Thus, the 30% or more increase in PM2.5 concentrations in Figure 20c between 13 and 20 July suggests that air in the free troposphere over Cape Cod must have frequently encountered deep convection upwind over North America. The model results also show that the parameterized convection does not affect the height and depth of aerosol layers significantly over Cape Cod but does modulate the aerosol concentrations in those layers and yields results close to the observations in the case of the Maritime Column.

To further illustrate how vertical transport and aqueous chemistry within parameterized clouds influences aerosol concentrations over Cape Cod, Figure S16 shows the percentage change in CO, BC, $SO_4 < 2.5\,\mu m$, and $SO_4 > 2.5\,\mu m$ between the simulations with and without KF-CuP. CO can be considered an inert tracer, and Figure S16a shows that the inclusion of vertical transport in parameterized clouds leads to lower concentrations in the boundary layer and higher concentrations aloft. The largest differences usually occur in the upper troposphere and are due to deep convection. BC is also a scalar; however, it is internally mixed with other aerosol species and is affected by wet removal. Consequently, the differences in BC between the two simulations (Figure S16b) are similar to the pattern shown in Figure 20c. Differences in fine-mode SO_4 (Figure S16c) are also similar to BC and PM, although the simulation with KF-CuP has somewhat lower concentrations since a portion of the mass has moved into the coarse mode via aqueous chemistry as indicated by the large increases shown in Figure S16d. The percentage change in coarse mode SO_4 is large and frequently exceeds 60%, but the concentrations of coarse mode SO_4 are small (usually $<0.1\,\mu g\,m^{-3}$). Thus, aqueous chemistry in parameterized convection behaves in the same way as resolved clouds as described by *Chapman et al.* [2009].

4. Discussion

It is important to note that there are uncertainties in the AMS and SP2 measurements shown in Figures 10 and 16 that should be considered when assessing the performance of simulated aerosol composition concentrations. For the AMS, most of the uncertainties are associated with its collection efficiency that has been reported to be highly variable, ranging from unity to 15% [*Docherty et al.*, 2013]. Aerosol concentrations obtained by the AMS are corrected to account for the collection efficiency, but this correction is often not perfect and *Canagaratna et al.* [2007] report an overall uncertainty of 25%. One should also treat low concentrations, often observed in the free troposphere or in pristine conditions, with caution as well. Under controlled laboratory experiments, *Drewnick et al.* [2009] found that the lower detection limit of the time-of-flight AMS to be $0.003\,\mu g\,m^{-3}$ for nitrate and sulfate and $0.03\,\mu g\,m^{-3}$ for organic matter and ammonium; however, the detection limit may be higher in ambient conditions. *Schwarz et al.* [2010b] report uncertainties in BC concentrations from the SP2 to be 25%. While these uncertainties in aerosol concentrations are relatively large, they do not affect the overall conclusions regarding processes affecting the vertical distribution of aerosols.

Our results show that the higher upward vertical motions associated with midlatitude synoptic-scale systems in the regional WRF-Chem simulations produces a better representation of aerosol layers in the free troposphere with higher aerosol concentrations than in CAM5. Since CAM5 has coarser spatial resolution, it has weaker convergence and hence weaker upward vertical motions. Thus, CAM5 in the configuration used in

this study does not transport aerosols upward as high as observed or as found in the WRF-Chem simulations. The performance of global climate models in simulating the vertical distribution of aerosols will likely improve as they use much smaller grid spacings in the future. For example, *Ma et al.* [2014] used WRF-Chem to show increases in peak BC concentrations and their spatial variability over the Pacific Ocean when the grid spacing is reduced from 160 to 10 km. In addition to decreasing the horizontal grid spacing, decreasing the vertical grid spacing is also needed to resolve the observed vertical variations in aerosol concentrations. The number of vertical levels typically used in global climate models, including this study, is often low compared to mesoscale models because of the computational constraints arising from the need for long simulation periods. However, the relatively coarse grid spacing in the middle troposphere leads to much smoother aerosol profiles than observed during TCAP (e.g., Figures 8c and 14c).

Note that we cannot attribute all of CAM5's underestimation of aerosols in the free troposphere to just resolution and vertical transport. The SOA treatment in the default version of CAM5 is simple where most of the SOA forms close to the surface and it does not include multigenerational chemistry of S/IVOC precursors. *Shrivastava et al.* [2015] showed that a more complex SOA treatment that explicitly simulates multigenerational chemistry of SOA improved the vertical distribution of organic aerosols. Since organic aerosols often comprise the largest fraction of fine particulate matter, the treatment of chemistry in CAM5 could also contribute to the underestimation of total aerosol mass in the free troposphere.

While higher spatial resolution will lead to more realistic aerosol distributions, evaluating aerosol predictions becomes problematic since small transport errors can lead to large differences in the observed and simulated profiles. While a model may be predicting realistic aerosol distributions using higher spatial resolution, from a statistical point of view the performance could be poor. This issue has been widely recognized in the meteorological modeling community [e.g., *Mass et al.*, 2002], but it also applies to aerosol predictions. For example, the free troposphere aerosol layer on 17 July in WRF-Chem arrives too soon and about 1 km too high. On 22 July, the residual layer aerosol concentrations in WRF-Chem are too low because the band of higher concentrations is located just northwest of the aircraft flight path, whereas the residual layer is better in CAM5 because the large grid spacing averages out the regional variability over the Gulf of Maine. Global climate models already account for subgrid scale variability in clouds in some way by computing cloud fractions and probability density functions of cloud properties. Less attention has been placed on accounting for subgrid variability in aerosols, and similar methodologies will be useful as global climate models.

In terms of climate modeling, errors in the simulated aerosol layers will have an impact on local aerosol radiative forcing. In particular, the simulated profile of black carbon and dust will affect heating rate profiles and ultimately the evolution of clouds [e.g., *Koch and Del Genio*, 2010]. The altitude of the aerosol layers in the free troposphere is also important in terms of the indirect effect since the altitude of the aerosol layer will affect whether aerosols are entrained into clouds. Much attention has been placed on aerosol activation at cloud base where boundary layer aerosols are entrained into clouds by rising thermals; however, activation does not have to only occur at cloud base. For example, as deep convective clouds grow upward, they can entrain aerosol layers in the free troposphere and secondary activation can play an important role [*Yang et al.*, 2015]. Aerosol layers above clouds will also have an impact on radiative forcing [e.g., *Chand et al.*, 2009].

This study illustrates how the in situ and remote sensing measurements collected during TCAP can be used to evaluate both regional-scale and global model performance in a region just downwind of North America emission sources. It is important to understand the sources of model error in this region, since these errors will affect calculations of regional aerosol radiative forcing and the errors will ultimately propagate downwind to Europe and beyond within the context of a global model. In addition to transport and mixing processes that affect the vertical distribution of aerosols, data from the campaign can be used to evaluate SOA parameterizations that remain uncertain since the understanding of processes that contribute to the formation organic aerosols is incomplete. While we have shown the relative contribution of anthropogenic, biogenic, and biomass burning sources to total OM, the relative contribution from these sources may not be correct and the AMS and miniSPLAT measurements have not been analyzed to provide information regarding the types of organic aerosols observed. Our results show that more than half of the organic aerosol concentrations in the middle and upper troposphere originate from outside of North America from long-range transport; therefore, there is likely some uncertainty with the boundary conditions resulting from a coarse global model. Global

climate simulations that employ "regionally refined" domains will be subject to the same problem; therefore, higher spatial resolution is needed for the entire globe to adequately represent spatial variations of aerosols in the atmosphere.

5. Summary and Conclusions

A wide range of meteorological, trace gas, and aerosol measurements were collected by the TCAP campaign in the vicinity of Cape Cod during July 2012 and used to evaluate the performance of the WRF-Chem regional-scale and the CAM5 global models. In situ and remote sensing measurements revealed the presence residual layers resulting from aerosols within the continental boundary layer being transported over the ocean as well as layers above the residual layer in the free troposphere. The multiple layers produced large vertical variations in aerosol properties, but large horizontal variations within the layers were also observed. While the model performance is evaluated using all the aircraft flights conducted in July 2012, two periods (one dirty and one clean) are examined in detail to identify processes responsible for layers observed over the TCAP sampling domain. While neither model is perfect with regard to simulating all of the observed details of the aerosol layers, both models do reproduce the overall variability in aerosols observed on many days. We also examined the sensitivity of the simulated aerosol properties to a new convective parameterization that accounts for the vertical transport, aqueous chemistry, and wet removal within subgrid scale clouds. Our primary findings are as follows:

1. WRF-Chem produced higher aerosol concentrations and more distinct aerosol layers in the free troposphere than CAM5, so that the fraction of AOT above the residual layer was more consistent with the HSRL-2 data.
2. Analysis of the WRF-Chem simulations showed that the layers observed in the free troposphere are likely due to mean vertical motions associated with synoptic-scale convergence that lifts aerosols from the boundary. The vertical displacement and the time period associated with vertical transport depend on the strength of the synoptic system and whether higher aerosol concentrations are present where convergence occurs. For one case on 17 July, the lifting and higher wind speeds in the troposphere produces aerosols over the TCAP region that leads to aerosols less aged than aerosols in the residual layer.
3. Not surprisingly, mean upward vertical motions in the coarse CAM5 simulation are smaller those from WRF-Chem, which results in weak to nonexistent aerosol layers in the free troposphere in combination of wet removal that may be overestimated. Most of the aerosols simulated by CAM5 are located within 3 km of the surface over Cape Cod, whereas WRF-Chem produced periods of aerosol concentrations exceeding $3\,\mu g\,m^{-3}$ above 3 km during the dirty periods.
4. In general, the PM1 concentration and extinction profiles from WRF-Chem were too low compared to the in situ and remote sensing measurements, although the performance varied from day to day. The flights on 17 and 25 July were the only days with substantial overpredictions in PM1.
5. In contrast to WRF-Chem, simulated PM1 from CAM5 was usually too high in the residual layer. The simulated extinction in the residual layer was closer to observed than WRF-Chem but still lower than observed in spite of the overprediction in PM1. The low bias in extinction profiles is consistent with the low bias in AOD at the Cape Cod site.
6. Simulated surface concentrations of PM1 at the Cape Cod site were too high in CAM5 because of the high SOA yield applied at the surface, and with the large grid spacing, one grid box encompasses the site and both portions of Boston.
7. Underpredictions in RH, particularly near the top of the residual layer and in the lower troposphere likely contributed to part of the low bias in the simulated extinction profiles of both models.
8. BC concentrations simulated by both models was too large at the surface and aloft, suggesting that the emission inventory estimates may be too high.
9. On average, about 50, 30, and 10% of the OM simulated by WRF-Chem below 2 km is from anthropogenic, biogenic, and biomass burning sources, although these fractions varied substantially during the simulation period. Simulated biomass burning aerosol concentrations were similar in magnitude to the observations except during the clean periods when total OM concentrations were low and the simulated biomass burning aerosol concentrations were too high.
10. A sensitivity simulation using WRF-Chem showed that the effects of parameterized convective clouds on aerosols modulated the concentrations of the aerosol layers, but did not significantly change the overall

altitude and depth of the layers. While parameterized convection transports aerosols from the boundary layer into the free troposphere, wet removal is an effective sink so that the net effect of parameterized clouds is to reduce aerosol concentrations over the TCAP sampling region.

Our objective was not to determine which model performed better, but to illustrate the types of uncertainties in simulating aerosol models that are different in spatial resolution and complexity in the treatment of aerosols. The present evaluation shows how two key processes transport by mean vertical motions and convective clouds that are coupled over multiple days need to be better represented in models. The TCAP data were very valuable in this regard.

In the future, simulations by both models using smaller horizontal and vertical grid spacing could be conducted to determine what resolution and domain size is needed to adequately simulate these layers. Global climate models are beginning to use regionally refined domains that have coarse resolution over the globe with finer resolution over the domain of interest. This is similar to the nested grid approach used by mesoscale models, such as WRF, except that the transition between coarse and fine grid spacing is gradual. Our results show that errors in the coarse domain could produce layers at the wrong altitude that would be transported into the regions of finer resolution. While a regionally refined domain is likely to produce better simulation of local processes such as clouds, we show that it will not solve all of the climate-relevant issues associated with scale.

References

Angevine, W. M., M. Tjernstrom, and M. Zagar (2006), Modeling of the coastal boundary layer and pollutant transport in New England, *J. Appl. Meteorol. Climatol.*, *138*, 137–154.

Barth, M. C., et al. (2007), Cloud-scale model intercomparison of chemical constituent transport in deep convection, *Atmos. Chem. Phys.*, *7*, 4709–4731.

Barth, M. C., et al. (2015), The Deep Convective Clouds and Chemistry (DC3) field campaign, *Bull. Am. Meteorol. Soc.*, *96*, 1281–1309, doi:10.1175/BAMS-D-13-00290.1.

Berg, L. K., and R. B. Stull (2005), A simple parameterization coupling the convective daytime boundary layer and fair-weather cumuli, *J. Atmos. Sci.*, *62*, 1976–1988, doi:10.1175/jas3437.

Berg, L. K., et al. (2009), Overview of the Cumulus Humilis Aerosol Processing Study, *Bull. Am. Meteorol. Soc.*, *90*, 1653–1667, doi:10.1175/2009BAMS2760.1.

Berg, L. K., W. I. Gustafson, E. I. Kassianov, and L. Deng (2013), Evaluation of a modified scheme for shallow convection: Implementation of CuP and case studies, *Mon. Weather Rev.*, *141*, 134–147, doi:10.1175/mwr-d-12-00136.1.

Berg, L. K., M. Shrivastava, R. C. Easter, J. D. Fast, E. G. Chapman, and Y. Liu (2015), A new WRF-Chem treatment for studying regional scale impacts of cloud-aerosol interactions in parameterized cumuli, *Geophys. Model Dev.*, *8*, 409–429, doi:10.5194/gmd-8-409-2015.

Berg, L. K., et al. (2016), The Two-Column Aerosol Project: Phase I—Overview and impact of elevated aerosol layers on aerosol optical depth, *J. Geophys. Res. Atmos.*, *121*, 336–361, doi:10.1002/2015JD023848.

Bond, T. C., et al. (2013), Bounding the role of black carbon in the climate system: A scientific assessment, *J. Geophys. Res. Atmos.*, *118*, 5380–5552, doi:10.1002/jgrd.50171.

Brioude, J., et al. (2013), The Lagrangian particle dispersion model FLEXPART-WRF VERSION 2.1, *Geophys. Model Dev.*, *6*, 1889–1904.

Canagaratna, M. R., et al. (2007), Chemical and microphysica characterization of ambient aerosols with the aerodyne aerosol mass spectrometer, *Mass Spectrom. Rev.*, *26*, 185–222, doi:10.1002/mas.20115.

Carter, W. P. L. (2000a), Documentation of the SAPRC-99 Chemical Mechanism for VOC Reactivity Assessment, Draft report to the California Air Resources Board. Contracts 92–329 and 95–308, 8 May. [Available at http://www.cert.ucr.edu/_carter/absts.htm#saprc99.]

Carter, W. P. L. (2000b), Implementation of the SAPRC-99 Chemical Mechanism into the Models-3 Framework, Report to the United States Environmental Protection Agency, 29 January. [Available at http://www.cert.ucr.edu/_carter/absts.htm#s99mod3.]

Chand, D., R. Wood, T. L. Anderson, S. K. Satheesh, and R. J. Charlson (2009), Satellite-derived direct radiative effect of aerosols dependent on cloud cover, *Nat. Geosci.*, *2*, 181–184, doi:10.1038/ngeo437.

Chapman, E. G., W. I. Gustafson, R. C. Easter, J. C. Barnard, S. J. Ghan, M. S. Pekour, and J. D. Fast (2009), Coupling aerosol-cloud-radiative processes in the WRF-Chem model: Investigating the radiative impact of elevated point sources, *Atmos. Chem. Phys.*, *9*, 945–964.

Coburn, S., B. Dix, R. Sinreich, and R. Volkamer (2011), The CU ground MAX-DOAS instrument: Characterization of RMS noise limitations and first measurements near Pensacola, FL of BrO, IO, and CHOCHO, *Atmos. Meas. Tech.*, *4*, 2421–2439, doi:10.5194/amt-4-2421-2011.

Cooper, O. R., et al. (2004), A case study of transpacific warm conveyor belt transport: Influence of merging airstreams on trace gas import to North America, *J. Geophys. Res.*, *109*, D23S08, doi:10.1029/2003JD003624.

Croft, B., J. R. Pierce, R. V. Martin, C. Hoose, and U. Lohmann (2012), Uncertainty associated with convective wet removal of entrained aerosols in a global climate model, *Atmos. Chem. Phys.*, *12*, 10,725–10,748, doi:10.5194/acp-12-10725-2012.

Dacre, H. F., S. L. Gray, and S. E. Belcher (2007), A case study of boundary layer ventilation by convection and coastal processes, *J. Geophys. Res.*, *112*, D17106, doi:10.1029/2006JD007984.

Dacre, H. F., A. L. M. Grant, N. J. Harvey, D. J. Thomson, H. N. Webster, and F. Marenco (2015), Volcanic ash layer depth: Processes and mechanisms, *Geophys. Res. Lett.*, *42*, 637–645, doi:10.1002/2014GL062454.

De Wekker, S. F. J., and M. Kossmann (2015), Convective boundary layer heights over mountainous terrain - A review of concepts, *Front. Earth Sci.*, *3*, 77, doi:10.3389/feart.2015.00077.

DeCarlo, P. F., et al. (2006), A field-deployable high-resolution time-of-flight aerosol mass spectrometer, *Anal. Chem.*, *78*, 8281–8289.

Docherty, K. S., M. Jaoui, E. Corse, J. L. Jimenez, J. H. Offenburg, M. Lewandowski, and T. E. Kliendienst (2013), Collection efficiency of the Aerosol Mass Spectrometer for chamber-generated secondary organic aerosols, *Aerosol Sci. Technol.*, *47*, 294–309, doi:10.1080/02786826.2012.752572.

Drewnick, F., S. S. Hings, M. R. Alfarra, A. S. H. Prevot, and S. Borrmann (2009), Aerosol quantification with the Aerodyne Aerosol Mass Spectrometer: Detection limits and ionizer background effects, *Atmos. Meas. Tech.*, *2*, 33–46, doi:10.5194/amt-2-33-2009.

Emmons, L. K., et al. (2010), Description and evaluation of the Model for Ozone and Related chemical Tracers, version 4 (MOZART-4), *Geosci. Model Dev.*, *3*, 43–67, doi:10.5194/gmd-3-43-2010.

Esler, J. G., P. H. Haynes, K. S. Law, H. Barjat, K. Dewey, J. Kent, S. Schmitgen, and N. Brough (2003), Transport and mixing between airmasses in cold frontal regions during Dynamics and Chemistry of Frontal Zones (DCFZ), *J. Geophys. Res.*, *108*(D4), 4142, doi:10.1029/2001JD001494.

Fast, J. D., W. I. Gustafson Jr., R. C. Easter, R. A. Zaveri, J. C. Barnard, E. G. Chapman, and G. A. Grell (2006), Evolution of ozone, particulates, and aerosol direct forcing in an urban area using a new fully-coupled meteorology, chemistry, and aerosol model, *J. Geophys. Res.*, *111*, D21305, doi:10.1029/2005JD006721.

Fast, J. D., et al. (2009), Evaluating simulated primary anthropogenic and biomass burning organic aerosols during MILAGRO: Implications for assessing treatments of secondary organic aerosols, *Atmos. Chem. Phys.*, *9*, 6196–6215, doi:10.5194/acp-9-6191-2009.

Fast, J. D., et al. (2014), Modeling regional aerosol variability over California and its sensitivity to emissions and long-range transport during the 2010 CalNex and CARES campaigns, *Atmos. Chem. Phys.*, *14*, 10,013–10,060, doi:10.5194/acp-14-10013-2014.

Feng, Y., V. R. Kotamarthi, R. Coulter, C. Zhao, and M. Cadeddu (2016), Radiative and thermodynamic responses to aerosol extinction profiles during the pre-monsoon month over South Asia, *Atmos. Chem. Phys.*, *16*, 247–264, doi:10.5194/acp-16-247-2016.

Gerken, T., et al. (2016), Downward transport of ozone rich air and implications for atmospheric chemistry in the Amazon rainforest, *Atmos. Environ.*, *124*, 64–76, doi:10.1016/j.atmosenv.2015.11.014.

Gettelman, A., H. Morrison, and S. J. Ghan (2008), A new two-moment bulk stratiform cloud microphysics scheme in the NCAR Community Atmosphere Model (CAM3), Part II: Single-column and global results, *J. Clim.*, *21*, 3660–3679.

Gettelman, A., X. Liu, S. J. Ghan, H. Morrison, S. Park, A. J. Conley, S. A. Klein, J. Boyle, D. L. Mitchell, and J.-L. F. Li (2010), Global simulations of ice nucleation and ice supersaturation with an improved cloud scheme in the Community Atmosphere Model, *J. Geophys. Res.*, *115*, D18216, doi:10.1029/2009JD013797.

Ghan, S. J., X. Liu, R. C. Easter, R. Zaveri, P. J. Rasch, J.-H. Yoon, and B. Eaton (2012), Toward a minimal representation of aerosols in climate models: Comparative decomposition of aerosol direct, semidirect, and indirect radiative forcing, *J. Clim.*, *25*, 6461–6476, doi:10.1175/JCLI-D-11-00650.1.

Ginoux, P., M. Chin, I. Tegen, J. M. Prospero, B. Holben, O. Dubovik, and S.-J. Lin (2001), Sources and distributions of dust aerosols simulated with the GOCART model, *J. Geophys. Res.*, *106*, 20,255–20,273, doi:10.1029/2000JD000053.

Gong, S. L., L. A. Barrie, and M. Lazare (2002), Canadian Aerosol Module (CAM): A size-segregated simulation of atmospheric aerosol processes for climate and air quality models, 2. Global sea-salt aerosol and its budgets, *J. Geophys. Res.*, *107*(D24), 4779, doi:10.1029/2001JD002004.

Grell, G. A., S. E. Peckham, R. Schmitz, S. A. McKeen, G. Frost, W. C. Skamarock, and B. Eder (2005), Fully coupled "online" chemistry within the WRF model, *Atmos. Environ.*, *39*, 6957–6975.

Guenther, A., T. Karl, P. Harley, C. Wiedinmyer, P. I. Palmer, and C. Geron (2006), Estimates of global terrestrial isoprene emissions using MEGAN (Model of Emissions of Gases and Aerosols from Nature), *Atmos. Chem. Phys.*, *6*, 3181–3210.

Gustafson, W. I., E. G. Chapman, S. J. Ghan, R. C. Easter, and J. D. Fast (2007), Impact on modeled cloud characteristics due to simplified treatment of uniform cloud condensation nuclei during NEAQS 2004, *Geophys. Res. Lett.*, *34*, L19809, doi:10.1029/2007GL030021.

Hair, J. W., C. A. Hostetler, A. L. Cook, D. B. Harper, R. A. Ferrare, T. L. Mack, W. Welch, L. R. Izquierdo, and F. E. Hovis (2008), Airborne High Spectral Resolution Lidar for profiling aerosol optical properties, *Appl. Opt.*, *47*, 6734–6752.

Heald, C. L., et al. (2011), Exploring the vertical profile of atmospheric organic aerosol: Comparing 17 aircraft field campaigns with a global model, *Atmos. Chem. Phys.*, *11*, 12,673–12,696, doi:10.5194/acp-11-12673-2011.

Hodzic, A., P. S. Kasibhatla, D. S. Jo, C. Cappa, J. L. Jimenez, S. Madronich, and R. J. Park (2015), Rethinking the global secondary organic aerosol (SOA) budget: Stronger production, faster removal, shorter lifetime, *Atmos. Chem. Phys. Discuss.*, *15*, 32,413–32,468, doi:10.5194/acpd-15-32413-2015.

Horowitz, L., et al. (2003), A global simulation of tropospheric ozone and related tracers: Description and evaluation of MOZART, version 2, *J. Geophys. Res.*, *108*(D24), 4784, doi:10.1029/2002JD002853.

Im, U., et al. (2015), Evaluation of operational online-coupled regional air quality models over Europe and North America in the context of AQMEII phase 2. Part II: Particulate matter, *Atmos. Environ.*, *115*, 421–441, doi:10.1016/j.atmosenv.2014.08.072.

Jayne, J. T., D. C. Leard, X. Zhang, P. Davidovits, K. A. Smith, C. E. Kolb, and D. R. Worsnop (2000), Development of an aerosol mass spectrometer for size and composition analysis of submicron particles, *Aerosol Sci. Technol.*, *33*, 49–70, doi:10.1080/027868200410840.

Kain, J. S. (2004), The Kain-Fritsch convective parameterization: An update, *J. Appl. Meteorol.*, *43*, 170–181, doi:10.1175/1520-0450(2004)043<0170:tkcpau>2.0.co;2.

Kain, J. S., and J. M. Fritsch (1990), A one-dimensional entraining detraining plume model and its application in convective parameterization, *J. Atmos. Sci.*, *47*, 2784–2802, doi:10.1175/1520-0469(1990)047<2784:aodepm>2.0.co;2.

Kassianov, E., J. Barnard, M. Pekour, L. K. Berg, J. Michalsky, K. Lantz, and G. Hodges (2013), Do diurnal aerosol changes affect daily average radiative forcing?, *Geophys. Res. Lett.*, *40*, 3265–3269, doi:10.1002/grl.50567.

Kassianov, E., et al. (2015), Airborne Aerosol in Situ Measurements during TCAP: A Closure Study of Total Scattering, *Atmosphere*, *6*, 1069–1101, doi:10.3390/atmos6081069.

Kipling, Z., et al. (2016), What controls the vertical distribution of aerosol? Relationships between process sensitivity in HadGEM3–UKCA and inter-model variation from AeroCom Phase II, *Atmos. Chem. Phys.*, *16*, 2221–2241, doi:10.5194/acp-16-2221-2016.

Koch, D., and A. D. Del Genio (2010), Black carbon semi-direct effects on cloud cover: Review and synthesis, *Atmos. Chem. Phys.*, *10*, 7685–7696, doi:10.5194/acp-10-7685-2010.

Koffi, B., et al. (2012), Application of the CALIOP layer product to evaluate the vertical distribution of aerosols estimated by global models: AeroCom phase I results, *J. Geophys. Res.*, *117*, D10201, doi:10.1029/2011JD016858.

Kooperman, G. J., M. S. Pritchard, S. J. Ghan, M. Wang, R. C. J. Somerville, and L. M. Russell (2012), Constraining the influence of natural variability to improve estimates of global aerosol indirect effects in a nudged version of the Community Atmosphere Model 5, *J. Geophys. Res.*, *117*, D23204, doi:10.1029/2012JD018588.

Liu, H., et al. (2006), Radiative effect of clouds on tropospheric chemistry in a global three-dimensional chemical transport model, *J. Geophys. Res.*, *111*, D20303, doi:10.1029/2005JD006403.

Liu, X., et al. (2012), Toward a minimal representation of aerosols in climate models: Description and evaluation in the Community Atmosphere Model CAM5, *Geosci. Model Dev.*, *5*, 709–739, doi:10.5194/gmd-5-709-2012.

Lu, R., and R. Turco (1994), Air pollutant transport in a coastal environment. Part I: Two-dimensional simulations of sea-breeze and mountain effects, *J. Atmos. Sci.*, *51*, 2285–2308.

Lugauer, M. U. B., M. Furger, H. W. Gaggeler, D. T. Jost, M. Schwikowski, and H. Wanner (1998), Aerosol transport to the high Alpine sites Jungfraujoch (3454 m asl) and Colle Gnifetti (4452 m asl), *Tellus, Ser. B, 50,* 76–92.

Ma, H.-Y., C. C. Chuang, S. A. Klein, M.-H. Lo, Y. Zhang, S. Xie, X. Zheng, P.-L. Ma, Y. Zhang, and T. J. Phillips (2015), An improved hindcast approach for evaluation and diagnosis of physical processes in global climate models, *J. Adv. Model. Earth Syst., 7,* 1810–1827, doi:10.1002/2015MS000490.

Ma, P.-L., P. J. Rasch, J. D. Fast, R. C. Easter, W. I. Gustafson Jr., X. Liu, S. J. Ghan, and B. Singh (2014), Assessing the CAM5 physics suite in the WRF-Chem model: Implementation, resolution sensitivity, and a first evaluation for a regional case study, *Geosci. Model Dev., 7,* 755–778, doi:10.5194/gmd-7-755-2014.

Mass, C. F., D. Ovens, and K. Westrick (2002), Does Increasing Horizontal Resolution Produce More Skillful Forecasts?, *Bull. Am. Meteorol. Soc., 83,* 407–430.

Mather, J. H., and J. W. Voyles (2013), The ARM Climate Research Facility: A review of structure and capabilities, *Bull. Am. Meteorol. Soc., 94*(3), 377–392, doi:10.1175/BAMS-D-11-00218.1.

McKendry, I. G., J. P. Hacker, R. Stull, S. Sakiyama, D. Mignaccaand, and K. Reid (2001), Long-range transport of Asian dust to the Lower Fraser Valley, British Columbia, Canada, *J. Geophys. Res., 106,* 18,361–18,370, doi:10.1029/2000JD900359.

Morrison, H., and A. Gettelman (2008), A new two-moment bulk stratiform cloud microphysics scheme in the Community Atmosphere Model, Version 3 (CAM3). Part I: Description and numerical tests, *J. Clim., 21,* 3642–3659, doi:10.1175/2008JCLI2105.1.

Moteki, N., and Y. Kondo (2007), Effects of mixing state on black carbon measurements by laser-induced incandescence, *Aerosol Sci. Technol., 41,* 398–417, doi:10.1080/02786820701199728.

Müller, D., et al. (2014), Airborne Multiwavelength High Spectral Resolution Lidar (HSRL-2) observations during TCAP 2012: Vertical profiles of optical and microphysical properties of a smoke/urban haze plume over the northeastern coast of the US, *Atmos. Meas. Tech., 7,* 3487–3496, doi:10.5194/amt-7-3487-2014.

Myhre, G., et al. (2013), Radiative forcing of the direct aerosol effect from AeroCom Phase II simulations, *Atmos. Chem. Phys., 13,* 1853–1877, doi:10.5194/acp-13-1853-2013.

Neale, R. B., et al. (2010), Description of the NCAR community atmosphere model (CAM 5.0) NCAR Tech. Note NCAR/TN-486+ STR.

Ng, N. L., et al. (2011), An Aerosol Chemical Speciation Monitor (ACSM) for routine monitoring of the composition and mass concentrations of ambient aerosol, *Aerosol Sci. Technol., 45,* 780–794, doi:10.1080/02786826.2011.560211.

Ortega, I., T. Koenig, R. Sinreich, D. Thomson, and R. Volkamer (2015), The CU 2-D-MAX-DOAS instrument—Part 1: Retrieval of 3-D distributions of NO2 and azimuth-dependent OVOC ratios, *Atmos. Meas. Tech., 8,* 2371–2395, doi:10.5194/amt-8-2371-2015.

Ortega, I., S. Coburn, L. K. Berg, K. Lantz, J. Michalsky, R. Ferrare, J. Hair, C. Hostetler, and R. Volkamer (2016), The CU 2D-MAX-DOAS instrument - part 2: Raman Scattering Probability Measurements and Retrieval of Aerosol Optical Properties, *Atmos. Meas. Tech. Discuss.,* doi:10.5194/amt-2015-385.

Park, S., and C. S. Bretherton (2009), The University of Washington shallow convection and moist turbulence schemes and their impact on climate simulations with the Community Atmosphere Model, *J. Clim., 22,* 3449–3469.

Parrish, D. D., J. S. Holloway, R. Jakoubek, M. Trainer, T. B. Ryerson, G. Hübler, F. C. Fehsenfeld, J. L. Moody, and O. R. Cooper (2000), Mixing of anthropogenic pollution with stratospheric ozone: A case study from the North Atlantic wintertime troposphere, *J. Geophys. Res., 105,* 24,363–24,374.

Reidmiller, D. R., D. A. Jaffe, D. Chand, S. Strode, P. Swartzendruber, G. M. Wolfe, and J. A. Thornton (2009), Interannual variability of long-range transport as seen at the Mt. Bachelor observatory, *Atmos. Chem. Phys., 9,* 557–572.

Samset, B. H., et al. (2013), Black carbon vertical, profiles strongly affect its radiative forcing uncertainty, *Atmos. Chem. Phys., 13,* 2423–2434, doi:10.5194/acp-13-2423-2013.

Schmid, B., et al. (2014), The DOE ARM Aerial Facility, *Bull. Am. Meteorol. Soc., 95*(5), 723–742, doi:10.1175/bams-d-13-00040.1.

Schulz, M., et al. (2006), Radiative forcing by aerosols as derived from the AeroCom present-day and pre-industrial simulations, *Atmos. Chem. Phys., 6,* 5225–5246.

Schwarz, J. P., et al. (2006), Single-particle measurements of midlatitude black carbon and light-scattering aerosols from the boundary layer to the lower stratosphere, *J. Geophys. Res., 111,* D16207, doi:10.1029/2006JD007076.

Schwarz, J. P., J. R. Spackman, R. S. Gao, L. A. Watts, P. Stier, M. Schulz, S. M. Davis, S. C. Wofsy, and D. W. Fahey (2010a), Global-scale black carbon profiles observed in the remote atmosphere and compared to models, *Geophys. Res. Lett., 37,* L18812, doi:10.1029/2010GL044372.

Schwarz, J. P., et al. (2010b), The detection efficiency of the Single Particle Soot Photometer, *Aerosol Sci. Technol., 44,* 612–628, doi:10.1080/02786826.2010.481298.

Schwarz, J. P., B. H. Samset, A. E. Perring, J. R. Spackman, R. S. Gao, P. Stier, M. Schulz, F. L. Moore, E. A. Ray, and D. W. Fahey (2013), Global-scale seasonally resolved black carbon vertical profiles over the Pacific, *Geophys. Res. Lett., 40,* 5542–5547, doi:10.1002/2013GL057775.

Shrivastava, M., J. D. Fast, R. C. Easter, W. I. Gustafson Jr., R. A. Zaveri, A. Hodzic, and J. Jimenez (2011), Modeling organic aerosols in a megacity: Comparison of simple and complex representations of the volatility basis set approach, *Atmos. Chem. Phys., 11,* 6639–6662.

Shrivastava, M., A. Zelenyuk, D. Imre, R. Easter, J. Beranek, R. A. Zaveri, and J. D. Fast (2013), Implications of low volatility SOA and gas-phase fragmentation reactions on SOA loadings and their spatial and temporal evolution in the atmosphere, *J. Geophys. Res. Atmos., 118,* 3328–3342, doi:10.1002/jgrd.50160.

Shrivastava, M., et al. (2015), Global transformation and fate of SOA: Implications of low-volatility SOA and gas-phase fragmentation reactions, *J. Geophys. Res. Atmos., 120,* doi:10.1002/2014JD022563.

Smith, S. J., J. van Aardenne, Z. Klimont, R. J. Andres, A. Volke, and S. Delgado Arias (2011), Anthropogenic sulfur dioxide emissions: 1850-2005, *Atmos. Chem. Phys., 11,* 1101–1116, doi:10.5194/acp-11-1101-2011.

Sprenger, M., and H. Wernli (2015), The LAGRANTO Lagrangian analysis tool – version 2.0, *Geosci. Model Dev., 8,* 2569–2586, doi:10.5194/gmd-8-2569-2015.

Stroud, C. A., et al. (2011), Impact of model grid spacing on regional- and urban- scale air quality predictions of organic aerosol, *Atmos. Chem. Phys., 11,* 3107–3118, doi:10.5194/acp-11-3107-2011.

Stull, R. B. (1988), *An Introduction to Boundary Layer Meteorology,* Kluwer Acad., Dordrecht.

Textor, C., et al. (2006), Analysis and quantification of the diversities of aerosol life cycles within AeroCom, *Atmos. Chem. Phys., 7,* 1777–1813, doi:10.5194/acp-6-1777-2006.

Thalman, R., and R. Volkamer (2010), Inherent calibration of a blue LED-CE-DOAS instrument to measure iodine oxide, glyoxal, methyl glyoxal, nitrogen dioxide, water vapour and aerosol extinction in open cavity mode, *Atmos. Meas. Tech., 3,* 1797–1814, doi:10.5194/amt-3-1797-2010.

Thalman, R., et al. (2015), Instrument intercomparison of glyoxal, methyl glyoxal and NO2 under simulated atmospheric conditions, *Atmos. Meas. Tech., 8,* 1835–1862, doi:10.5194/amt-8-1835-2015.

Titos, G., A. Jefferson, P. J. Sheridan, E. Andrews, H. Lyamani, L. Alados-Arboledas, and J. A. Ogren (2014), Aerosol light-scattering enhancement due to water uptake during the TCAP campaign, *Atmos. Chem. Phys.*, *14*, 7031–7043, doi:10.5194/acp-14-7031-2014.

Tsigaridis, K., et al. (2014), The AeroCom evaluation and intercomparison of organic aerosol in global models, *Atmos. Chem. Phys.*, *14*, 10,845–10,895, doi:10.5194/acp-14-10845-2014.

Tsimpidi, A. P., V. A. Karydis, M. Zavala, W. Lei, L. Molina, I. M. Ulbrich, J. L. Jimenez, and S. N. Pandis (2010), Evaluation of the volatility basis-set approach for the simulation of organic aerosol formation in the Mexico City metropolitan area, *Atmos. Chem. Phys.*, *10*(2), 525–546.

Verma, S., O. Boucher, C. Venkataraman, M. S. Reddy, D. Muller, P. Chazette, and B. Crouzille (2006), Aerosol lofting from sea breeze during the Indian Ocean Experiment, *J. Geophys. Res.*, *111*, D07208, doi:10.1029/2005JD005953.

Wainwright, C. D., J. R. Pierce, J. Liggio, K. B. Strawbridge, A. M. Macdonald, and R. W. Leaitch (2012), The effect of model spatial resolution on Secondary Organic Aerosol predictions: A case study at Whistler, BC, Canada, *Atmos. Chem. Phys.*, *12*, 10,911–10,923, doi:10.5194/acp-12-10911-2012.

Walter, C., S. R. Freitas, C. Kottmeier, I. Kraut, D. Rieger, H. Vogel, and B. Vogel (2016), The importance of plume rise on the concentrations and atmospheric impacts of biomass burning aerosol, *Atmos. Chem. Phys.*, *16*, 9201–9219, doi:10.5194/acp-16-9201-2016.

Wang, H., R. C. Easter, P. J. Rasch, M. Wang, X. Liu, S. J. Ghan, Y. Qian, J.-H. Yoon, P.-L. Ma, and V. Vinoj (2013), Sensitivity of remote aerosol distributions to representation of cloud–aerosol interactions in a global climate model, *Geosci. Model Dev.*, *6*, 765–782, doi:10.5194/gmd-6-765-2013.

Wiedinmyer, C., S. K. Akagi, R. J. Yokelson, L. K. Emmons, J. A. Al-Saadi, J. J. Orlando, and A. J. Soja (2011), The Fire INventory from NCAR (FINN): A high resolution global model to estimate the emissions from open burning, *Geosci. Model Dev.*, *4*, 625–641, doi:10.5194/gmd-4-625-2011.

Wofsy, S. C., et al. (2011), HIAPER pole-to-pole observations (HIPPO): Fine-grained, global-scale measurements of climatically important atmospheric gases and aerosols, *Philos. Trans. R. Soc., A*, *369*, 2073–2086, doi:10.1098/rsta.2010.0313.

Yang, Q., et al. (2015), Aerosol transport and wet scavenging in deep convective clouds – a case study and model evaluation based on a severe storm during the DC3 campaign, *J. Geophys. Res. Atmos.*, *120*, 8448–8468, doi:10.1002/2015JD023647.

Zarzycki, C. M., and T. C. Bond (2010), How much can the vertical distribution of black carbon affect its global direct radiative forcing?, *Geophys. Res. Lett.*, *37*, L20807, doi:10.1029/2010GL044555.

Zaveri, R. A., R. C. Easter, J. D. Fast, and L. K. Peters (2008), Model for Simulating Aerosol Interactions and Chemistry (MOSAIC), *J. Geophys. Res.*, *113*, D13204, doi:10.1029/2007JD008782.

Zelenyuk, A., J. Yang, E. Choi, and D. Imre (2009), SPLAT II: An aircraft compatible, ultra-sensitive, high precision instrument for in-situ characterization of the size and composition of fine and ultrafine particles, *Aerosol Sci. Technol.*, *43*, 411–424, doi:10.1080/02786820802709243.

Zelenyuk, A., D. Imre, J. Wilson, Z. Zhang, J. Wang, and K. Mueller (2015), Airborne Single Particle Mass Spectrometers (SPLAT II & miniSPLAT) and new software for data visualization and analysis in a geo-spatial context, *J. Am. Soc. Mass Spectrom.*, *26*, 257–270, doi:10.1007/s13361-014-1043-4.

Zhang, G. J., and N. A. McFarlane (1995), Sensitivity of climate simulations to the parameterization of cumulus convection in the Canadian climate centre general circulation model, *Atmos. Ocean*, *33*, 407–446.

Zhang, K., H. Wan, X. Liu, S. J. Ghan, G. J. Kooperman, P.-L. Ma, P. J. Rasch, D. Neubauer, and U. Lohmann (2014), Technical Note: On the use of nudging for aerosol–climate model intercomparison studies, *Atmos. Chem. Phys.*, *14*, 8631–8645, doi:10.5194/acp-14-8631-2014.

Zhang, X., S. Kondragunta, J. Ram, C. Schmidt, and H.-C. Huang (2012), Near-real-time global biomass burning emissions product from geostationary satellite constellation, *J. Geophys. Res.*, *117*, D14201, doi:10.1029/2012JD017459.

Zhao, C., X. Liu, L. R. Leung, B. Johnson, S. McFarlane, W. I. Gustafson Jr., J. D. Fast, and R. Easter (2010), The spatial distribution of dust and its short wave radiative impact over North Africa: Modeling sensitivity to dust emissions and aerosol size treatments, *Atmos. Chem. Phys.*, *10*, 8821–8838.